Icarus 203 (2009) 437–453

Contents lists available at ScienceDirect

Icarus

journal homepage: www.elsevier.com/locate/icarus

Mineralogical characterization of Mars Science Laboratory candidate landing sites from THEMIS and TES data

A. Deanne Rogers [a,*], Joshua L. Bandfield [b]

[a] Department of Geosciences, Stony Brook University, 255 Earth and Space Sciences Building, Stony Brook, NY 11794-2100, USA
[b] Department of Earth and Space Sciences, University of Washington, Johnson Hall 070, Box 351310, 4000 15th Avenue NE, Seattle, WA 98195-1310, USA

ARTICLE INFO

Article history:
Received 9 January 2009
Revised 14 April 2009
Accepted 24 April 2009
Available online 13 May 2009

Keywords:
Mars, Surface
Mineralogy

ABSTRACT

Data from the Mars Global Surveyor Thermal Emission Spectrometer (TES) and the Mars Odyssey Thermal Emission Imaging System (THEMIS) instruments are used to assess the mineralogic and dust cover characteristics of landing regions proposed for the Mars Science Laboratory (MSL) mission. Candidate regions examined in this study are Eberswalde crater, Gale crater, Holden crater, Mawrth Vallis, Miyamoto crater, Nili Fossae Trough, and south Meridiani Planum. Compositional units identified in each region from TES and THEMIS data are distinguished by variations in hematite, olivine, pyroxene and high-silica phase abundance, whereas no units are distinguished by elevated phyllosilicate or sulfate abundance. Though phyllosilicate minerals have been identified in all sites using near-infrared observations, these minerals are not unambiguously detected using either TES spectral index or deconvolution analysis methods. For some of the sites, small phyllosilicate outcrop sizes relative to the TES field of view likely hinder phyllosilicate mineral detection. Porous texture and/or small particle size (<~60 μm) associated with the phyllosilicate-bearing surfaces may also contribute to non-detections in the thermal infrared data sets, in some areas. However, in Mawrth Vallis and Nili Fossae, low phyllosilicate abundance (<10–20 areal %, depending on the phyllosilicate composition) is the most likely explanation for non-detection. TES data over Mawrth Vallis indicate that phyllosilicate-bearing surfaces also contain significant concentrations (>15%, possibly up to ~40%) of a high-silica phase such as amorphous silica or zeolite. High-silica phase abundance over phyllosilicate-bearing surfaces in Mawrth Vallis is higher than that of surrounding surfaces by 10–15%. With the exception of these high-silica surfaces in Mawrth Vallis, regions examined in this study exhibit similar bulk mineralogical compositions to that of most low-albedo regions on Mars; the MSL scientific payload will thus be able to provide important information on surface materials typical of low-albedo regions in addition to investigating the origin of phyllosilicate and/or sulfate deposits. With the exception of Gale crater, all of the landing sites have relatively low dust cover compared to classic high-albedo regions (Tharsis, Arabia and Elysium) and to previous landing sites in Gusev Crater, Utopia Planitia, and Chryse Planitia.

1. Introduction

The Mars Science Laboratory (MSL) is a roving robotic spacecraft planned for launch in 2011. MSL mission objectives are to locate and interpret evidence of the environmental history of a region of Mars, particularly with respect to characterizing past or present habitability. The design of MSL allows for considerably relaxed constraints on landing site selection compared to those for the Mars Exploration Rovers (Golombek et al., 2003), with an allowable latitude range of 45°S to 30°N, altitudes as high as 1 km above the areoid, and landing ellipses as small as 25 km along the major elliptical axis (http://marsoweb.nas.nasa.gov/landingsites/index.html). In early 2006, the Mars scientific community was solicited for candidate landing site suggestions. Since that time, more than 30 sites have been proposed in response to the initial call. During the course of three open workshops held in June 2006, October 2007, and September 2008, candidate landing site regions were prioritized and down-selected on the basis of (1) morphologic and spectroscopic evidence for aqueous activity and/or habitable environment from existing orbital data, (2) mineralogic diversity, (3) likelihood that surface materials encountered by MSL will be easily placed into a more regional context observed from orbit, and (4) potential for biosignature preservation (http://marsoweb.nas.nasa.gov/landingsites/msl2009/memoranda/sites_jul08/Discussion%20Points-Science%20Criteria.doc). At the conclusion of the September 2008 workshop, the final sites under consideration were: Eberswalde crater, Gale crater, Holden crater, Miyamoto crater, Nili Fossae Trough, south Meridiani Planum,

* Corresponding author.
E-mail addresses: adrogers@notes.cc.sunysb.edu (A.D. Rogers), joshband@u.washington.edu (J.L. Bandfield).

0019-1035/$ - see front matter © 2009 Elsevier Inc. All rights reserved.
doi:10.1016/j.icarus.2009.04.020

and four separate locations in Mawrth Vallis (Table 1). In November 2008, the MSL landing site steering committee further reduced the list of candidate landing sites to Gale crater, Holden crater, Eberswalde crater, and ellipse number two in Mawrth Vallis. In the months leading up to the launch of MSL, a single landing region will be selected from these top four sites. A final landing site workshop will also be held to choose a specific landing ellipse location within that region (http://marsoweb.nas.nasa.gov/landingsites/index.html).

Our work uses data from the Mars Global Surveyor Thermal Emission Spectrometer (TES) and the Mars Odyssey Thermal Emission Imaging System (THEMIS) to assess the mineralogic characteristics and dust cover contribution for the top seven candidate landing regions reviewed at the September 2008 workshop. This work was carried out under directive from the MSL program to (1) facilitate selection of the site with the highest possible scientific potential by maximizing the mineralogical understanding of candidate regions, as well as to (2) provide context while the mission is in progress. These thermal infrared (TIR) analyses are highly complementary to ongoing near-infrared (NIR) measurements of each site from the Mars Express Observatoire pour la Minéralogie, l'Eau, les Glaces, et l'Activité (OMEGA) (Bibring et al., 2005) and Mars Reconnaissance Orbiter Compact Reconnaissance Imaging Spectrometer for Mars (CRISM) (Murchie et al., 2007) instruments. This paper does not address the detailed NIR spectral characteristics or thermophysical properties of the candidate sites; these aspects are the subjects of ongoing work by other researchers (Fergason, R., 2008. Thermal Inertia Maps of Candidate MSL Landing Sites, presentation at the 3rd MSL Landing Site Workshop, Monrovia, CA. Available from: <http://marsoweb.nas.nasa.gov/landingsites/msl2009/workshops/3rd_workshop/program.html/>; Seelos et al., 2008; Michalski and Fergason, 2009).

The data sets, processing, and analysis methods used in this work are described first below. Then for each site, a brief overview of the science rationale behind its candidacy and an analysis of the mineralogical and dust cover characteristics are given. Sites are presented in order of increasing east longitude. Data products generated for this work are currently available in raw format at http://faculty.washington.edu/joshband/cdp/index.html.

2. Data and methods

2.1. THEMIS and TES instrument descriptions

The THEMIS infrared subsystem is a multispectral imager with ~100 m/pixel spatial sampling and a swath width of ~32 km. The infrared imager measures radiation at nine wavelengths between ~6.8 and 14.9 μm, with an average bandwidth of ~1 μm for each channel (Christensen et al., 2004). For each site, spectral units are identified from THEMIS IR data and their distributions are mapped at full spatial resolution (Section 2.2). Detailed mineralogical information is then determined for each spectral unit using TES data (Section 2.3).

The TES instrument measures infrared radiation between ~6 and 50 μm (1700–200 cm^{-1}) with a selectable spectral sampling of 5 or 10 cm^{-1}. The TES instrument also contains a visible bolometer that measures lambert albedo between ~0.3 and 3.0 μm. Each detector footprint covers an area of ~3 × 8 km (Christensen et al., 1992, 2001). In this work, the TES data are used to perform quantitative mineralogical analyses (Section 2.3) and spectral feature mapping (Sections 2.4 and 2.5) for each site. The TES hyperspectral, low-spatial resolution data may be used in combination with THEMIS data to provide detailed mineralogic information at a high-spatial resolution.

2.2. Spectral unit maps

For each candidate site, THEMIS daytime radiance images with warm average surface temperatures (>245 K) are corrected for atmospheric dust and water ice contributions and converted to emissivity using the methods described by Bandfield et al. (2004). Atmospherically corrected THEMIS images are then mosaicked together, with a spatial resolution of 100 m per pixel. Decorrelation stretched (DCS) (Gillespie et al., 1986) emissivity images are used to identify spectral end-members within each candidate landing region. Average spectra from each end-member surface are extracted from each image in the mosaic. Those spectra are then normalized to the mean spectral contrast and averaged to obtain a representative spectral shape for that end-member surface. The normalization to average spectral contrast results in some surfaces exhibiting modeled concentrations greater than 1.0 in the spectral unit maps.

Once spectral end-members are identified, spectral unit maps are generated from surface emissivity mosaics using a spectral library that includes the end-members plus spectra appropriate for a given landing site (Sections 3–9). A linear least-squares fitting algorithm (Ramsey and Christensen, 1998) is used to model each THEMIS pixel using the spectral library (Bandfield et al., 2004), resulting in concentration distributions of each spectral unit. Unlike DCS mosaics, these maps provide quantitative information about the fractional contribution of each end-member to the surface emissivity on a pixel-by-pixel basis. In addition, information from the full spectral range is utilized and interfering atmospheric and temperature effects are minimized.

Table 1
Candidate MSL landing sites analyzed in this study.

Site name	Approximate center latitude/longitude coordinates of proposed landing ellipse(s)
Nili Fossae Trough	21.01°N, 74.45°E
Gale crater	4.49°S, 137.42°E
Holden crater	26.38°S, 325.08°E
Eberswalde crater	23.86°S, 326.73°E
Mawrth Vallis	24.65°N, 340.1°E, 23.99°N, 341.04°E, 23.21°N, 342.43°E, 24.85°N, 339.42°E
Miyamoto crater	3.51°S, 352.26°E
S. Meridiani Planum	3.05°S, 354.61°E

Table 2
TES data selection constraints.

	Surface emissivity derivation	Dust cover index
Target temperature, K	⩾255	⩾250
Emission angle	⩽30	⩽10
Orbit range[a]	1–5317	1–8504
Total ice extinction	⩽0.04	—
Total dust extinction	⩽0.15	—
Image motion compensation	None	None
Scan length (wave number spacing)	10	10
Quality: solar panel motion[b]	Unknown or <0.120 deg/s	None
Incidence angle	—	<80°

[a] MGS mapping phase orbit number. To convert to orbit counter keeper (OCK) number, add 1683.
[b] Additional quality and observational fields from the TES database used in this study: major_phase_inversion 0 0, algor_risk 0 0, spectral_mask 0 0 and detector_mask_problem 0 0. More information is available at http://pds-geosciences.wustl.edu/missions/mgs/tes.html.

2.3. Quantitative mineralogical analysis

TES emissivity spectra are extracted from areas exhibiting high concentrations of each spectral unit identified with THEMIS data. To ensure analysis of high quality spectra with minimal atmospheric contributions and spectral artifacts, TES database query fields and selection parameters given in Table 2 are used. Spectra from individual orbits are averaged and corrected for atmospheric effects using the linear least-squares fitting method described by Bandfield et al. (2000a) and Smith et al. (2000). The least-squares fitting algorithm used is a modified version of the non-negative least-squares method of Lawson and Hanson (1974), as described by Rogers and Aharonson (2008), and the spectral library used is given in Table 3. Where possible, surface emissivity is derived from multiple orbits with varying atmospheric conditions in order to build confidence in the derived surface emissivity shape for each unit (e.g., Rogers et al., 2007). Mineral abundances and statistical uncertainties are derived from the average surface emissivity spectrum from each unit, again using the non-negative least-squares fitting routine described by Rogers and Aharonson (2008). Mineral abundances are summed within each compositional class and reported as group abundances (e.g., feldspar abundance, olivine abundance, Table 4). The group "high-silica phases" includes silica glass, opal, zeolite minerals, and phyllosilicate minerals. These phases cannot be reliably distinguished from one another in TES deconvolution models (e.g., Bandfield, 2002; Michalski et al., 2003; Michalski et al., 2005), particularly if individual constituents are present in low abundance.

Table 3
Spectral library[a].

	Quartz BUR-4120	Quartz
	Microcline BUR-3460	Alkali feldspar
	Albite WAR-0235 Oligoclase BUR-060D Andesine WAR-0024 Labradorite BUR-3080A Bytownite WAR-1384 Anorthite BUR-340	Plagioclase
	Bronzite NMNH-93527 Enstatite HS-9.4B Hypersthene NMNH-B18247	Orthopyroxene
(1)	Avg. Lindsley pigeonite	Low-Ca clinopyroxene
	Diopside WAR-6474 Augite NMNH-9780 Augite NMHN-122302 Hedenbergite manganoan DSM-HED01	High-Ca Clinopyroxene
	Forsterite BUR-3720A Fayalite WAR-RGFAY01	
(2)	KI 3362 Fo60	Olivine
(2)	KI 3115 Fo68	
(2)	KI 3373 Fo35	
(2)	KI 3008 Fo10	
	Biotite BUR-840 Muscovite WAR-5474 Serpentine HS-8.4B	
(3)	Illite Imt-1 <0.2 μm (pellet) Ca-montmorillonite solid STx-1	Phyllosilicates
(4)	Saponite (Eb-1?) <0.2 μm (pellet)	
(3)	SWy-1 <0.2 μm (pellet)	
(5)	K-rich glass	
(5)	SiO2 glass	Amorphous
(6)	opal-A (01-011)	Silica
(7)	Al-Opal	
	Magnesiohastingsite HS-115.4B Magnesiohornblende WAR-0354	Amphibole
(8)	Ave. Meridiani and Aram Hematite (TT derived)	Oxide
	Anhydrite ML-S9 Gypsum ML-S6	Sulfate
(9)	Kieserite	
	Calcite C40 Dolomite C20	Carbonate
(10)	Crystalline heulandite	Zeolite
(10)	Crystalline stilbite	

[a] Mineral spectra are from the ASU spectral library available online at http://tes.asu.edu (Christensen et al., 2000), with the following exceptions, denoted by numbers in parentheses before entries: (1) Wyatt et al. (2001); (2) Koeppen and Hamilton (2008); (3) Michalski et al. (2006); (4) Michalski et al. (2005); (5) Wyatt et al. (2001); (6) Michalski et al. (2003); (7) provided by M.D. Kraft; (8) Glotch et al. (2004); (9) provided by A.M. Baldridge; (10) spectra described in Ruff (2004).

2.4. TES dust cover index

The average emissivity between 1350 and 1400 cm^{-1} is a proxy for areal dust cover, where low values (<0.94) indicate high dust cover and high values (>0.97) indicate minimal dust cover (Ruff and Christensen, 2002). Dust cover index (DCI) values were derived from TES emissivity spectra selected using the database constraints given in Table 2. For each candidate landing site, DCI values were binned at a resolution of 16 pixels per degree and overlain on a THEMIS daytime radiance mosaic to provide morphological context.

2.5. TES 465 and 530 cm^{-1} indices

Phyllosilicate minerals have been identified in all of the candidate regions with OMEGA/CRISM data (e.g., Bibring et al., 2005; Poulet et al., 2005; Milliken, R.E., 2008. CRISM results for Eberswalde crater, presentation at the 3rd MSL Landing Site Workshop, Monrovia, CA. Available from: <http://marsoweb.nas.nasa.gov/ landingsites/msl2009/workshops/3rd_workshop/program.html/>; Mustard et al., 2008). Thus two spectral indices developed by Ruff and Christensen (2007) are used here to detect smectite clays in TES data. The 465 cm^{-1} spectral feature is present in the spectra of several phases with high Si/O ratios, such as clays, zeolites, amorphous silica, and high-silica glass, and also in hematite. Spectral features near ~530 cm^{-1} are present in some clays and in some primary igneous minerals found in basalts, such as olivine (Ruff and Christensen, 2007). High values of both spectral features (greater than 1.006 for the 465 cm^{-1} index and 1.005 for the 530 cm^{-1} index (Ruff and Christensen, 2007)) can be indicative of a "doublet" that is found in dioctahedral smectite clays, including montmorillonite, nontronite, and Fe-smectite. The indices were derived from TES emissivity spectra selected using the constraints described in Ruff and Christensen (2007), and binned at a resolution of 16 ppd for a $10 \times 10^{\circ}$ area surrounding each landing site. The clays measured for the ASU spectral library are in packed particulate and fine powdered forms (likely <~63 μm particle sizes). If the phyllosilicates on the surface are in a low-porosity form similar to the packed particulate samples in the ASU library (such as surface coatings), then they would have to be present in abundance greater than 10–20%, depending on the phyllosilicate composition, in order to produce positive detections of the smectite doublet in TES data (Ruff and Christensen, 2007). Smaller particle sizes or clays in loose form may be present at higher abundances (Ruff and Christensen, 2007).

Thus, though low abundances of phyllosilicate minerals cannot be reliably distinguished from other high-silica phases in deconvolution models, the indices do provide a specific, robust test for identifying local areas of elevated concentrations of dioctahedral smectite clays. These can be verified by ratios with spectrally featureless surfaces observed under the same atmospheric conditions (e.g., observations made at similar elevations and within the same orbit).

Table 4
TES-derived mineral abundances for non-dust spectral units in each candidate region[a].

	Feldspar	Pyroxene	Olivine	High-silica Phases	Sulfate	Hematite	Other
Nili Fossae Trough							
Basalt 1	33 ± 4	29 ± 5	9 ± 3	15 ± 4	6 ± 2	0	8
Basalt 2	32 ± 5	26 ± 5	6 ± 2	20 ± 4	9 ± 2	0	7
Gale crater							
Olivine basalt	20 ± 5	30 ± 9	15 ± 4	19 ± 5	12 ± 2	0	4
Holden							
Olivine basalt 1	24 ± 6	26 ± 6	18 ± 3	17 ± 5	10 ± 2	0	5
Olivine basalt 2	25 ± 6	33 ± 6	18 ± 5	7 ± 5	9 ± 2	0	8
Eberswalde crater							
Olivine basalt	22 ± 4	28 ± 5	12 ± 3	25 ± 5	9 ± 1	0	4
Mawrth Vallis							
Basalt 1	26 ± 7	31 ± 8	9 ± 5	18 ± 6	9 ± 4	3 ± 3	4
Basalt 2	27 ± 9	23 ± 12	0 ± 0	28 ± 9	6 ± 4	7 ± 4	8
Miyamoto							
Olivine basalt 1	21 ± 5	32 ± 4	13 ± 3	13 ± 4	15 ± 3	0	5
Olivine basalt 2	32 ± 6	26 ± 10	25 ± 6	5 ± 8	5 ± 2	0	7
Hematite-rich unit	17 ± 4	24 ± 4	5 ± 2	23 ± 8	12 ± 2	17 ± 1	3
South Meridiani Planum							
Olivine basalt	23 ± 6	36 ± 5	11 ± 3	13 ± 4	10 ± 2	0	4
Hematite-rich unit	19 ± 4	30 ± 4	10 ± 3	12 ± 4	9 ± 1	18 ± 1	3

[a] Abundances and absolute uncertainties are given in percents. Because the "other" group can contain compositionally and spectrally distinct components (amphibole, carbonate and quartz), uncertainties on the total abundance of "other" minerals are meaningless and therefore not given (e.g., Rogers and Aharonson, 2008).

2.6. TES hematite index

A spectral index developed for detecting crystalline hematite (Christensen et al., 2000a) is used to map hematite distributions. The index measures the depth of hematite spectral minima at ~300 and 450 cm^{-1} relative to a spectral maximum at ~375 cm^{-1}. Hematite spectral index maps are generated at a resolution of 16 ppd and presented in simple cylindrical projection.

3. Nili Fossae Trough

The Nili Fossae region contains abundant olivine-rich bedrock dissected by giant curvilinear fractures associated with the formation of Isidis Basin (Schultz and Frey, 1990; Hoefen et al., 2003; Hamilton and Christensen, 2005). Noachian-aged materials cut by the fractures contain layered units which are host to phyllosilicate minerals (Mustard et al., 2008). The extent and thickness of these units are consistent with sustained aqueous systems of moderate to alkaline pH (Mustard et al., 2008), suggesting high potential for past habitability. The proposed MSL landing ellipse is located on the floor of the largest Nili Fossae fracture, which also exhibits evidence of phyllosilicate minerals in CRISM data (Mustard, J.F., 2008. Mineralogic and Morphologic Diversity in Nili Trough, presentation at the 3rd MSL Landing Site Workshop, Monrovia, CA. Available from: <http://marsoweb.nas.nasa.gov/>). The area exhibits DCI values of 0.955–1.00, indicating relatively low dust cover compared to classic high-albedo regions on Mars (Tharsis, Arabia Terra, Elysium Planitia, DCI values typically <0.93).

The dominant THEMIS spectral unit in the region is spectrally intermediate between TES surface types 1 and 2 (Bandfield et al., 2000b) (Fig. 1). Lesser occurrences of a more mafic unit are found dispersed throughout the region. At THEMIS spectral resolution, the more mafic unit can be modeled as a combination of the dominant unit plus olivine. Thus for Nili Fossae, spectral unit maps were generated using an end-member library consisting of the dominant spectral unit type, olivine, average martian surface dust derived from TES data by Bandfield and Smith (2003), and blackbody. The spectral unit maps (Fig. 2) show that the dominant spectral unit is found throughout the region. Areas with higher abundance of the more mafic unit are located within the Nili Fossae Trough, but to the north and south of the proposed landing ellipse. Higher concentrations of the more mafic unit are also found in the plains eastward of the trough. Because the surface dust end-member is relatively featureless between ~8 and 12 μm, its distinction from the blackbody end-member is considered less reliable, and the distributions of these two end-members were combined. In the Nili Fossae region, spatial variations in blackbody/dust abundance may indicate varying surface dust abundance or particle size/textural variations within the other two spectral units.

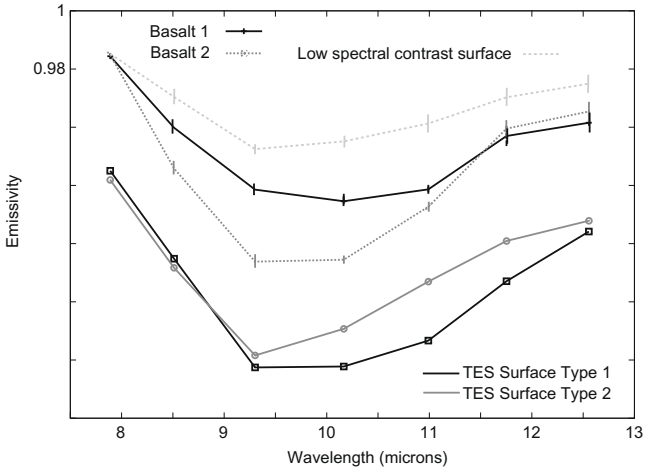

Fig. 1. THEMIS spectral end-members ("basalt 1" and "basalt 2", basalt 2 is the areally dominant unit) observed in the Nili Fossae Trough region. TES surface types 1 and 2 are shown for comparison. The "low spectral contrast" spectrum is taken from an area of relatively high dust/blackbody concentration in Fig. 2.

TES surface emissivity spectra were extracted from areas exhibiting high concentrations of each unit (Fig. 3). Using the TES-derived mineral abundances, both units are classified as basalt (Table 4). Both units do contain a significant amount of high-silica phases (15–20%), which may be secondary in origin. The less prevalent unit, "basalt 1" is spectrally distinct from "basalt 2",

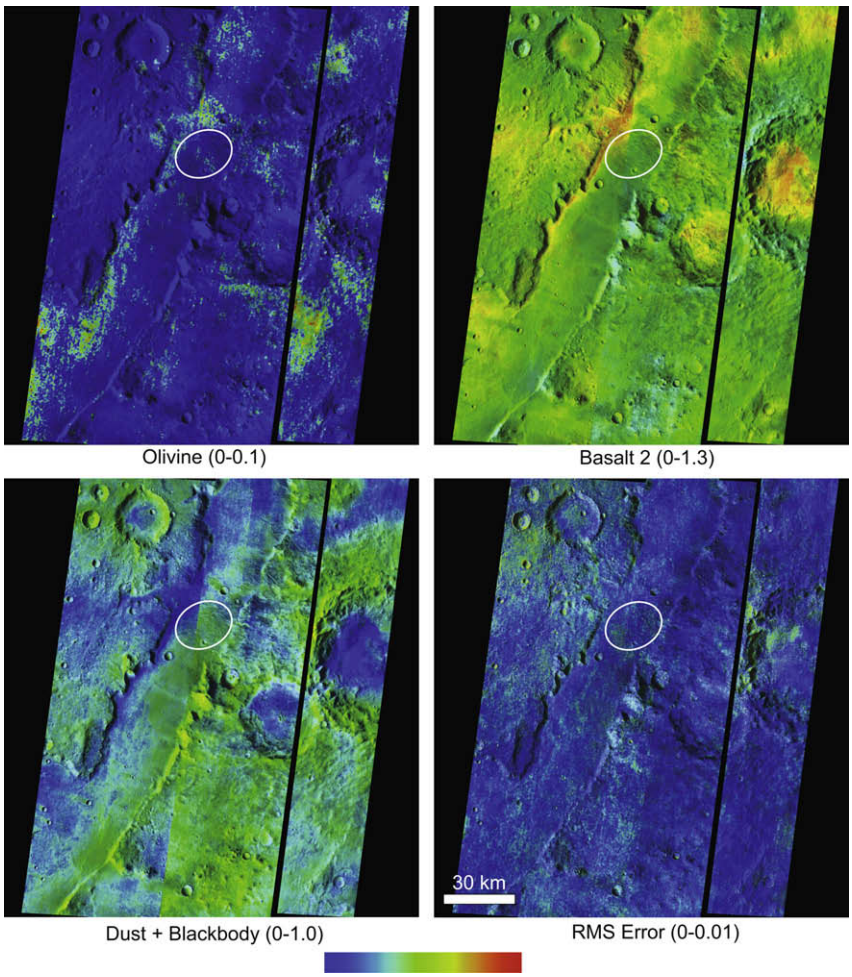

Fig. 2. THEMIS spectral unit distributions in the Nili Fossae Trough region. Each panel covers the area between 19° to 22°N and 73° to 76°E. The olivine map is a proxy for the distribution of basalt 1 (see text for explanation). All concentration values, shown in parentheses next to each map title, are relative to the spectral contrast of the end-members used for the spectral fitting. These values are meaningful only as relative indicators of surface concentration within the given image (Section 2.2). The white oval indicates the approximate location of the proposed primary landing ellipse.

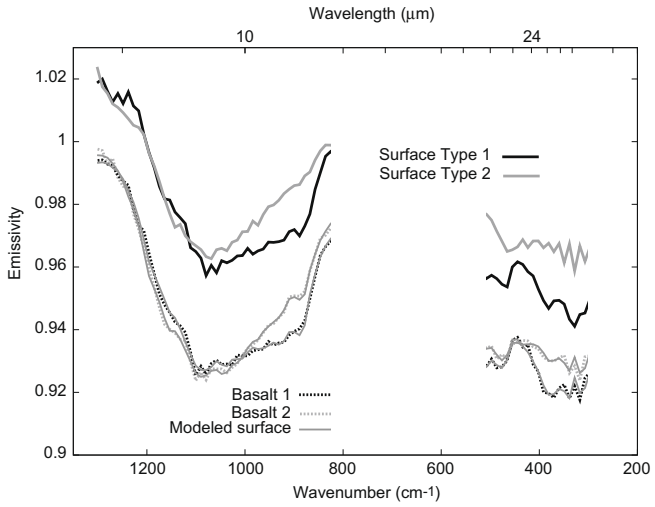

Fig. 3. TES surface emissivity spectra from the two major spectral units in the Nili Fossae Trough region. TES surface types 1 and 2 are shown for comparison and are offset by +0.02 emissivity.

and is similar to TES surface type 1 (Bandfield et al., 2000b). Though spectrally distinguishable from the basalt 2 unit, the derived mineral abundances are not significantly different than that of the basalt 2 unit. The slight differences in olivine, pyroxene, and high-silica phase abundances between the two basalt units are not greater the calculated errors associated with those abundances (Table 4). However, ratios of spectra from the basalt 1 and basalt 2 units confirm that their spectral differences may be primarily attributed to higher olivine and pyroxene abundance, and lower high-silica phase abundance in the basalt 1 unit compared to the basalt two unit. In summary, two spectral units are observed within the study area, which are both classified as basalts.

TES 465 cm^{-1} index values within the area covered by the THEMIS mosaic range from 0.995 to 1.017. TES 530 cm^{-1} index values range from 0.990 to 1.017 (Fig. 4). In the Nili Fossae region, high 530 cm^{-1} index values are primarily due to high concentrations of olivine in the area. There are a few areas which exhibit high values of both indices (1.01–1.02), which could indicate positive detections of phyllosilicate minerals. TES spectra were extracted from three of these areas. For two, ratios on and off of the surfaces with high 465 and 530 cm^{-1} index values do not show evidence of the smectite doublet. These false positives are likely orbit-specific artifacts; the 465 and 530 cm^{-1} features are present at slightly higher-than-neutral magnitudes throughout these orbits in this region, including surfaces which do not show evidence for phyllosilicates in OMEGA/CRISM data (Mustard et al., 2008). Because the 465 and 530 cm^{-1} features are present in both spectra used in

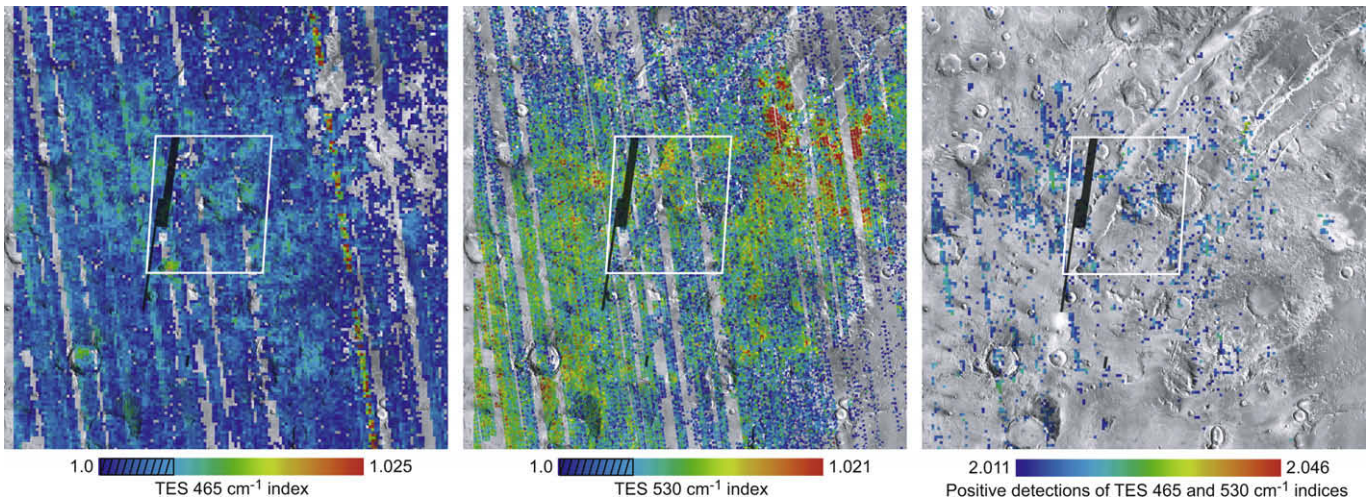

Fig. 4. TES 465 and 530 cm^{-1} index maps of the Nili Fossae Trough region (15–25°N, 70–80°E), overlaid on a THEMIS daytime radiance mosaic. The hatched portion of the color scale bar indicates values that are below the index detection thresholds established by Ruff and Christensen (2007) (1.006 for the 465 cm^{-1} index, 1.005 for the 530 cm^{-1} index). Maps of "positive detections" of both indices represent the sum value of both indices for each pixel, and are masked where either index is below their respective detection threshold. The white polygon shows the location of the spectral unit mosaics from Fig. 2.

the ratio, but only at slightly different magnitudes, the doublet does not appear in the ratio spectrum. For one orbit, a doublet is observed over the area in which both 465 and 530 cm^{-1} indices are high and in which phyllosilicate minerals were detected with OMEGA/CRISM (Mustard et al., 2008). The depth of the spectral features in the doublet (Fig. 5) are consistent with a ~15% increase of montmorillonite between the surface with high index values and the surface with low index values. However, the 530 cm^{-1} feature is co-located with a CO_2 hot band at ~535 cm^{-1}. The presence of a corresponding CO_2 hot band at ~788 cm^{-1} in the ratio spectrum suggests that the 530 cm^{-1} portion of the "doublet" is actually due to residual CO_2 in the ratio. This indicates that atmospheric conditions or the surface–atmosphere temperature contrast are not identical between the two surfaces used for this ratio. Thus the potential identification of phyllosilicates from TES data in this example is suspect. Explanations for the non-detections of smectite minerals in TES data include low abundance (<10–20%, depending on the phyllosilicate composition), and/or textural effects, such as small particle size. There are no apparent increases in blackbody concentration corresponding with NIR phyllosilicate identifications that would indicate decreased particle size or increased porosity (Fig. 2). This suggests that low phyllosilicate abundance is the most likely explanation. These results are consistent with mineral abundance estimates derived from OMEGA spectra for three select areas in Nili Trough (Poulet et al., 2008).

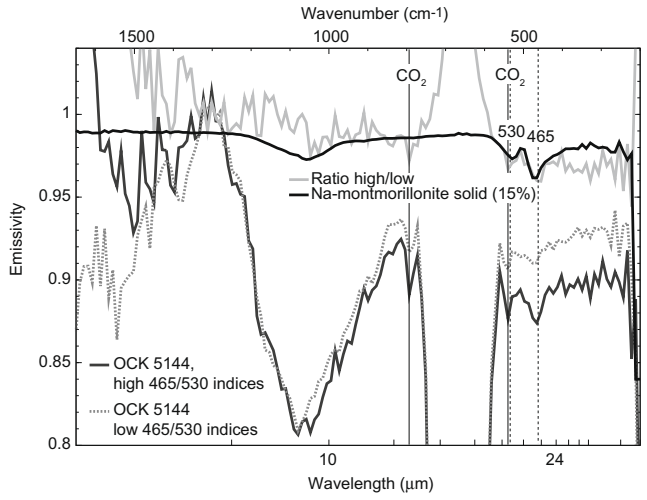

Fig. 5. Ratio of TES spectra from a surface with a "positive" 465 and 530 cm^{-1} index detection and a nearby surface with negative detections of both indices. The ratio is compared with a scaled montmorillonite spectrum. Locations of CO_2 "hot bands" at 535 and 788 cm^{-1} are indicated with vertical solid lines. The positions of 465 and 530 cm^{-1} are indicated with vertical dashed lines.

4. Gale crater

Gale crater hosts a ~5 km thick stack of layered units that record a history of repeated deposition and erosion in the region (Malin and Edgett, 2000). Bedforms and other features preserved in the section observed from orbit suggest possible subaqueous deposition for at least a portion of the stratigraphic section, and small exposures of phyllosilicate and sulfate minerals are detected with CRISM data in the lower portion of the section (Edgett, K., Milliken, R., Grotzinger, J., Malin, M., 2008. MSL Landing Sites: Gale, Reconsidered, MSL Steering Committee Presentations. Available from: <http://marsoweb.nas.nasa.gov/landingsites/>; Milliken et al., 2009). The detection of aqueous minerals within a thick stratigraphic context that can be mapped from orbit is one justification for Gale as a candidate landing site. An additional driver of the Gale campaign is that the sedimentary history preserved in the central mound may be representative of layered units (e.g., Vallis Marineris) and filled craters observed elsewhere on Mars. Also, the presence of a fan-like feature on the crater floor may present an opportunity to sample ancient rocks eroded from Gale's walls (Edgett, K., Milliken, R., Grotzinger, J., Malin, M., 2008. MSL Landing Sites: Gale, Reconsidered, MSL Steering Committee Presentations. Available from: <http://marsoweb.nas.nasa.gov/landingsites/>). The proposed landing ellipse is located in the northwest portion of the crater floor, with the ellipse boundary located adjacent to the layered units. The northern portion of a large dune field on the crater floor protrudes into the MSL landing ellipse area.

Compared to the other MSL candidate landing regions, TES albedo (~0.22) and DCI values (0.93–0.95) indicate relatively high dust cover. Though the dust cover is generally higher for this region, the detection of hydrated minerals with CRISM indicates that small portions of the crater mound must be less dust-covered.

THEMIS data were restricted to elevations near the crater floor because large elevation ranges within images interfere with the atmospheric correction. Spectral units identified in THEMIS observations of the crater floor include surface dust as well as a darker unit that is spectrally similar to TES surface type 1 (Bandfield et al., 2000b) but with a slightly deeper absorption at ~11 μm (Fig. 6). Spectral unit maps were produced using an image end-member from the dark unit, surface dust (Bandfield and Smith, 2003), and blackbody to account for variable spectral contrast. TES-derived surface emissivity spectra extracted from the darker unit are spectrally similar to TES surface type 1 (Fig. 7) (Bandfield et al., 2000b). TES-derived mineral abundances from the dark unit are consistent with an olivine basalt composition, although the unit also contains a significant amount of high-silica phases (~20%, Table 4), which may be secondary in origin. The olivine basalt composition is most strongly concentrated in the low-albedo dune field within Gale crater (Fig. 8). Outside of the dune field and within the proposed landing ellipse, the surface appears to be a mixture of the olivine basalt composition and surface dust. As was done for Nili Trough (Section 3), the surface dust and blackbody distributions of were combined. Spatial variations in blackbody/dust abundance may indicate varying surface dust abundance or particle size/textural variations within the olivine basalt spectral unit.

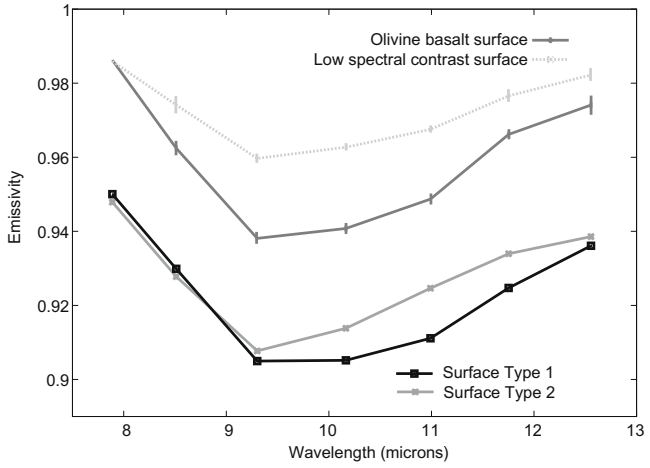

Fig. 6. THEMIS spectral end-member ("olivine basalt") observed in Gale crater. The "low spectral contrast" spectrum is taken from an area of relatively high dust/blackbody concentration in Fig. 8. TES surface types 1 and 2 are shown for comparison and are offset by −0.05 emissivity.

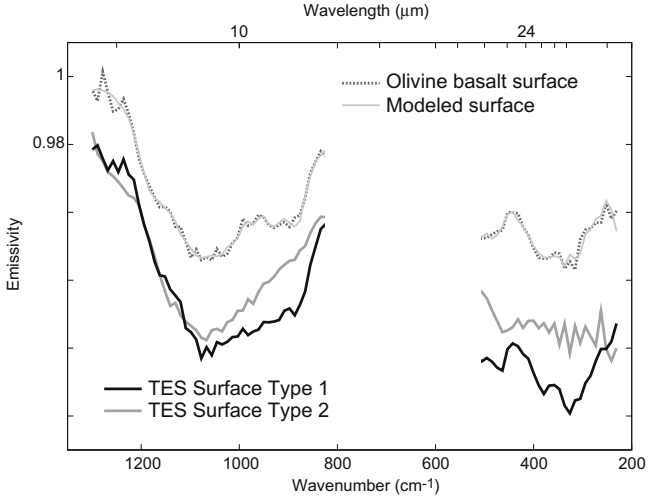

Fig. 7. TES surface emissivity spectrum from the olivine basalt unit in Gale crater. TES surface types 1 and 2 are shown for comparison and are offset by −0.02 emissivity.

In Gale crater, the 465 cm^{-1} spectral feature exhibits low values whereas the 530 cm^{-1} spectral feature exhibits low to moderate values associated with the low-albedo dune forms. The moderate 530 cm^{-1} index values are consistent with the olivine abundances estimated via least-squares modeling. Areas where both indices are present above the detection threshold are absent within the landing ellipse and generally sparse throughout the region. The lack of a smectite doublet in the TES 465 and 530 cm^{-1} index maps is likely partially due to small phyllosilicate outcrop size relative to the TES field of view (~3 × 8 km), but also may be attributed to (1) low phyllosilicate abundance (<10–20%, depending on the phyllosilicate composition), and/or (2) texture/particle size effects.

5. Holden crater

Holden, a ~150 km diameter crater located at ~324°E, 26°S, bisects the Uzboi–Ladon–Margaritifer Vallis outflow channel system. Where Uzboi Vallis breaches the southern rim of the crater, morphologic features consistent with alluvial fans are present (Malin and Edgett, 2000). Nearby layered units host phyllosilicate minerals, which are additional evidence for sustained aqueous activity (Grant et al., 2008).

As with Gale crater, THEMIS data were restricted to elevations near the crater floor because large elevation ranges within images interfere with the atmospheric correction. The floor of Holden crater consists of two basic spectral units in TES and THEMIS data (Figs. 9 and 10). The main unit is olivine basalt with a significant concentration of high-silica phases (~15%, Table 4) present. This is prevalent throughout much of the crater floor with the highest concentrations to the north and east of the landing ellipse (Fig. 11). The regions with high concentrations of this olivine basalt spectral signature often correspond with dune forms. These surfaces are likely to be self-abrading clean sands and relatively free of dust and small particulates, which would account for the relatively large spectral contrast present and corresponding large concentrations. Significant, but lower concentrations of this olivine basalt unit are present in the western and southern floor of the crater (including the landing ellipse) as well as within the valley that connects to the crater floor.

The second unit is much less prevalent with significant concentrations restricted to the southeast rim of a ~5 km diameter crater to the north of the landing ellipse and near the mouth of Uzboi Vallis (Fig. 11). This unit consists of similar plagioclase and olivine abundances to the more extensive olivine basaltic composition, but with less abundant high-silica phases and higher pyroxene abundances (Table 4). A deep spectral absorption between ~8 and 12 μm as well as high DCI values and low-albedo values indicate that little dust has accumulated throughout the Holden crater region. Unlike the Nili and Gale regions, the THEMIS-derived dust distribution exhibits some spatial coherency and thus was not combined with the blackbody distribution. It is possible that these dust and blackbody maps may be discriminating areas of increased dust cover from variations in particle size within the two olivine basalt units. Isolated areas with significant dust cover may be present in areas such as near the crater rim.

The prevalence of primary mafic minerals indicates that the surface materials are not highly altered in Holden crater. However, the high-silica phases present in the extensive olivine basaltic unit may indicate that some weathering/alteration has occurred throughout the region. The less extensive basaltic unit is likely to

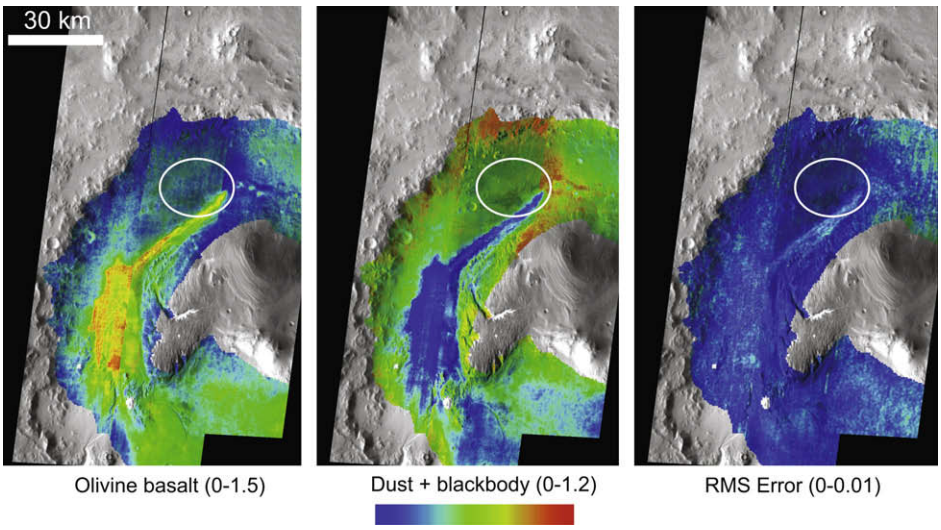

Fig. 8. THEMIS spectral unit distributions in Gale crater. Area shown is −6° to −3.5°N, 136.4° to 138.0°E. Map explanations are the same as in Fig. 2.

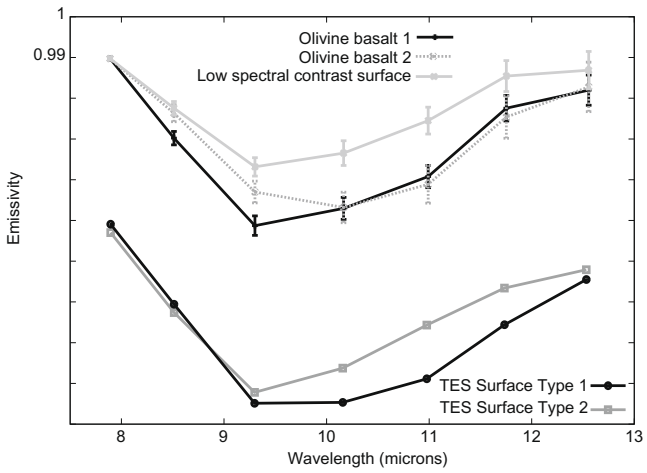

Fig. 9. THEMIS spectral end-members (“olivine basalt 1” and “olivine basalt 2”) observed in Holden crater. The “low spectral contrast” spectrum is taken from an area of relatively high dust/blackbody concentration in Fig. 11. TES surface types 1 and 2 are shown for comparison and are offset by −0.04 emissivity.

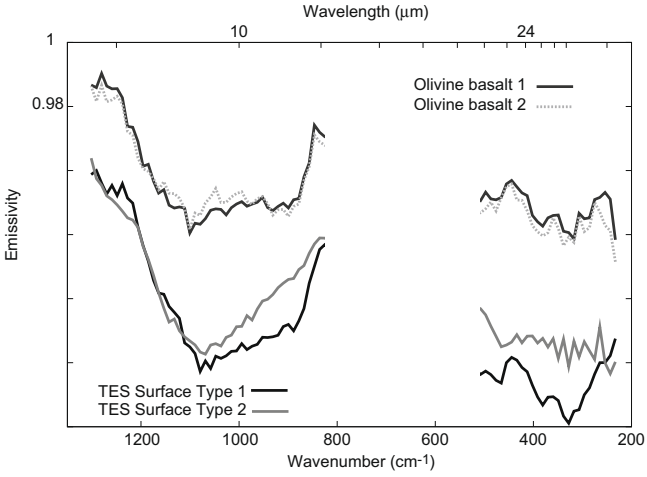

Fig. 10. TES surface emissivity spectra from the two major spectral units in Holden crater. TES surface types 1 and 2 are shown for comparison and are offset by −0.04 emissivity.

have had little, if any, alteration and is likely to be a relatively pristine igneous composition. This occurs near the mouth of Uzboi Vallis, but outside the region of distributary fan deposits.

Elevated 530 cm^{-1} index values are present near the landing ellipse, indicating significant olivine. The 465 cm^{-1} index values are low within the landing ellipse, though elevated values are present to the northeast where dune forms with high spectral contrast are present. As with Gale crater, the lack of a smectite doublet in TES data may be partially attributed to small phyllosilicate outcrop size relative to the TES field of view, but also may be due to low abundance and/or textural effects associated with the phyllosilicate-bearing materials.

6. Eberswalde crater

Eberswalde crater contains geomorphic features consistent with a deltaic complex, including layered units and meandering channels, implying deposition in a subaqueous environment (e.g., Malin and Edgett, 2003; Lewis and Aharonson, 2006). One of the primary goals of the MSL mission to Eberswalde would be to characterize the sedimentary sequence recorded in the layered units (Rice, J., Schieber, J., Milliken, R., Dickson, J., Edgett, K., Minitti, M., 2007. MSL Site: Eberswalde Deltaic Complex, Second MSL Landing Site Workshop Presentations. Available from: <http://marsoweb.nas.nasa.gov/landingsites/>), in addition to evaluating potential habitability. Phyllosilicate minerals have been tentatively identified with CRISM data in the deltaic complex and within the proposed landing ellipse (Milliken, R.E., 2008. CRISM Results for Eberswalde Crater, presentation at the 3rd MSL Landing Site Workshop, Monrovia, CA. Available from: <http://marsoweb.nas.nasa.gov/ landingsites/msl2009/workshops/3rd_workshop/program.html/>).

The proposed landing ellipse for Eberswalde contains relatively uniform DCI values of ~0.97, indicating relatively low dust cover. A single spectral unit (Fig. 12), which is similar to TES surface type 1 (Bandfield et al., 2000b), was identified in the region. Spectral unit maps were produced using this end-member as well as blackbody to account for variable spectral contrast (Fig. 13). Spatial variations in blackbody abundance may indicate small amounts of surface dust varying across the surface, or simply particle size variations within the surface type 1-like spectral unit. However in general, little variability in composition or spectral contrast is observed in THEMIS data. TES-derived surface emissivity spectra extracted

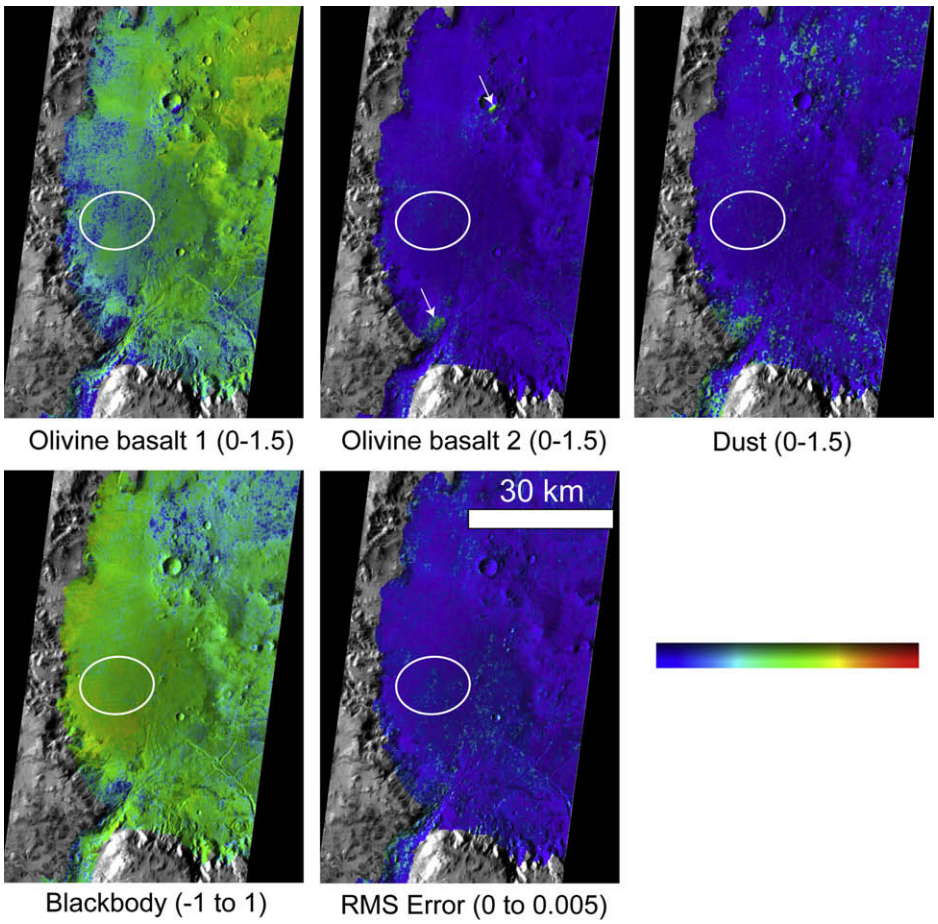

Fig. 11. THEMIS spectral spectral unit distributions in Holden crater. Area shown is −27.28° to −25.29°N, 324.46 to 326.0°E. White arrows point to main locations of olivine basalt 2, which are not easily visible at print scale. Map explanations are the same as in Fig. 2.

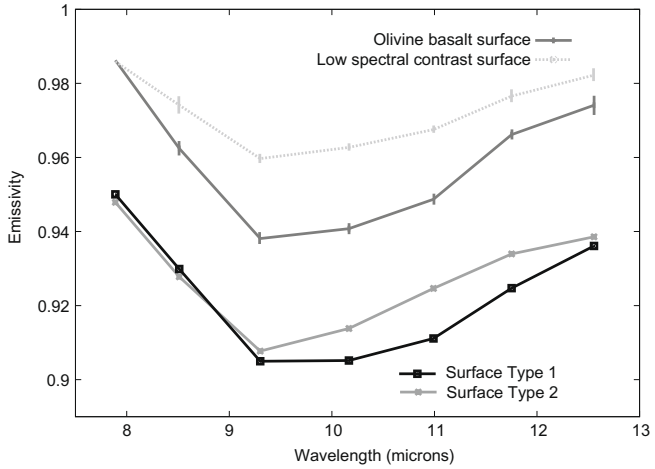

Fig. 12. THEMIS spectral end-member ("olivine basalt") observed in Eberswalde crater. The "low spectral contrast" spectrum is taken from an area of relatively high blackbody concentration in Fig. 13. TES surface types 1 and 2 are shown for comparison and are offset by −0.04 emissivity.

from the region are spectrally similar to TES surface type 1 (Bandfield et al., 2000b), with deep spectral contrast, consistent with the low dust cover indicated from DCI values. TES-derived mineral abundances are consistent with an olivine basalt composition, however the unit also contains a significant amount of high-silica phases (Table 4), which may be secondary in origin.

The TES 465 cm^{-1} index exhibits low to moderate values whereas the 530 cm^{-1} index exhibits moderate values within the crater. The moderate 530 cm^{-1} index values are consistent with the olivine abundance estimated via least-squares modeling; however, the low 465 cm^{-1} index values are not consistent with the ~25% modeled abundance of high-silica phases, suggesting that the high-silica abundance may have been slightly overestimated in the TES surface emissivity model. Minor under-correction for atmospheric components could cause an overestimation of high-silica phases. Areas where both the 465 and 530 cm^{-1} indices are present above the detection threshold are absent within the landing ellipse, indicating that the phyllosilicate minerals detected with CRISM are either (1) too small to be detected with TES data, (2) present in low abundance or (3) exist in high-porosity form, such as small loose particles.

7. Mawrth Vallis

Several extensive, continuous exposures of clay minerals were identified with OMEGA data in the region of Mawrth Vallis (Bibring et al., 2005; Poulet et al., 2005) (Fig. 14a). The deposits are associated with Noachian-aged materials and may be >600 m thick (Michalski and Dobrea, 2007). The presence of clay minerals is consistent with an environment of sustained aqueous activity and therefore relatively high potential for habitability. Given the wide areal exposure of clays in the Mawrth Vallis region, four candidate landing locations within the Mawrth Vallis region have been

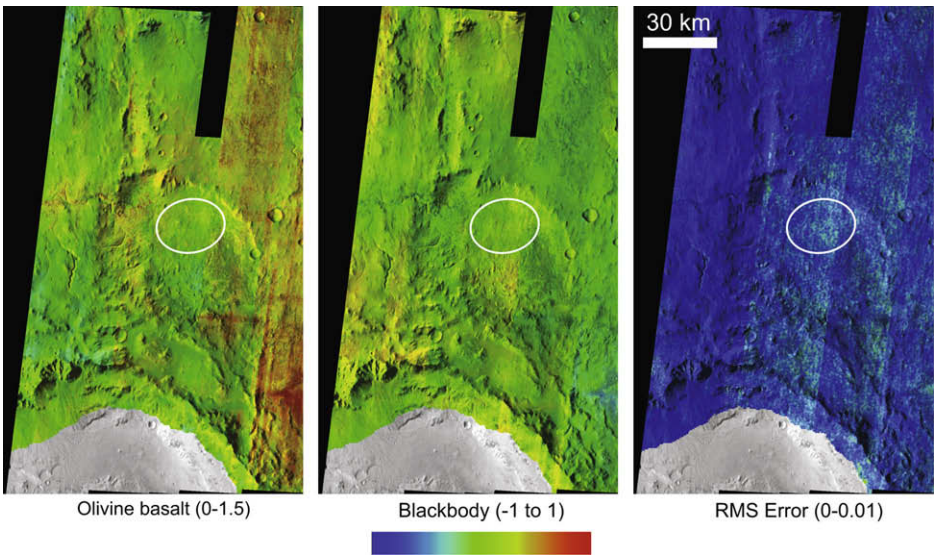

Fig. 13. THEMIS spectral unit distributions in Eberswalde crater. The TES dust cover index indicates dust cover is uniformly low throughout this region, thus no dust end-member was included in the spectral library for Eberswalde site. Area shown is −25.5° to −22.5°N, −34.5 to −32.5°E. Map explanations are the same as in Fig. 2.

proposed (Fig. 14a). Of these, ellipse numbers 1, 3 and 4 were removed from consideration as candidate landing sites at a down-selection meeting in November 2008.

In general, dust cover in the region is moderate to low, relative to classic high-albedo regions on Mars. Candidate landing ellipses 1–3 in Mawrth Vallis exhibit dust cover index values of 0.95–0.99, 0.94–1.00, and 0.94–0.99, respectively. TES data falling within the selection constraints are absent over candidate ellipse 4. The phyllosilicate minerals identified in NIR data are associated with light-toned units with 1.1 μm albedo values of ~0.18 (Poulet et al., 2005; Michalski and Dobrea, 2007; Mustard et al., 2008). The light-toned units do not exhibit significantly higher DCI values than surrounding units (with some exceptions), supporting the notion that the high-albedo value is an intrinsic property of the clay-bearing rocks (Michalski and Dobrea, 2007).

Two spectral units, which are spectrally similar to TES surface types 1 and 2 (Bandfield et al., 2000), were identified in THEMIS data (Figs. 14 and 15). The first unit can be modeled as the combination of the second unit plus olivine, therefore, spectral unit maps were produced using the second spectral unit, olivine, average martian surface dust derived from TES data by Bandfield and Smith (2003), and blackbody to account for variable spectral contrast (Fig. 14b). As with Nili Trough and Gale crater, the distributions of these last two end-members were combined. Spatial variations in blackbody/dust abundance may indicate varying surface dust abundance or particle size/textural variations within the other two spectral units.

TES-derived surface emissivity spectra extracted from the two units are spectrally similar to TES surface types 1 and 2 (Bandfield et al., 2000b), respectively (Fig. 16), and are distinguished primarily by differences in olivine and high-silica phase abundance. Using the TES-derived mineral abundances (Table 4), both units are classified as basalts and are referred to as "basalt 1" and "basalt 2". Both units contain a significant amount of high-silica phases (>15%, Table 4), which may be secondary in origin, thus both units may be altered. The basalt 2 unit contains a greater abundance of high-silica phases than the basalt 1 unit, however (Table 4).

The basalt 1 unit is concentrated near the western side of the study region (Fig. 14b), both in the plains that flank Mawrth Vallis, as well as in linear outcrops exposed at the base of the channel and in low-albedo deposits near the mouth of the channel. It is absent in the areas identified by OMEGA/CRISM as having positive detections of phyllosilicate minerals. The basalt 2 unit is found throughout the region, with some of the strongest concentrations associated with the phyllosilicate areas identified by OMEGA/CRISM (14). Though dust abundance is generally low throughout the study region, the THEMIS spectral unit maps do reveal variations in dust cover and/or particle size. Areas of higher dust/blackbody abundance are associated with light-toned outcrops where no phyllosilicates are observed by OMEGA/CRISM, as well as in plains to the east of Mawrth Vallis.

As described above, the basalt 2 unit contains the phyllosilicate surfaces identified in NIR measurements. Though the phyllosilicate-bearing surfaces are not distinct from other basalt 2 surfaces in THEMIS data, a spectral difference between phyllosilicate- and non-phyllosilicate-bearing regions is observed in TES data, particularly at wavelengths longward of 15 μm (Fig. 17). Deconvolution of TES spectra on and off the phyllosilicate regions reveal that the total high-silica phase abundance is higher than that of surrounding low-albedo surfaces by 10-15%. Aside from the difference in

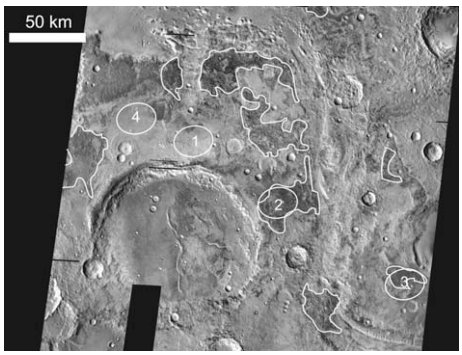

Fig. 14. (a) THEMIS daytime radiance mosaic of Mawrth Vallis region (22.5°N to 26°N, −22°E to −17°E). Approximate locations of phyllosilicate-bearing materials identified from OMEGA data are outlined in white. Approximate locations of proposed primary ellipses are also outlined in white. Dark tones represent cooler surfaces whereas lighter tones represent warmer surfaces. In Mawrth Vallis, cooler regions correspond with higher albedo surfaces. (b) THEMIS spectral unit distributions in the Mawrth Vallis region. Area shown is the same in (a). Map explanations are the same as in Fig. 2.

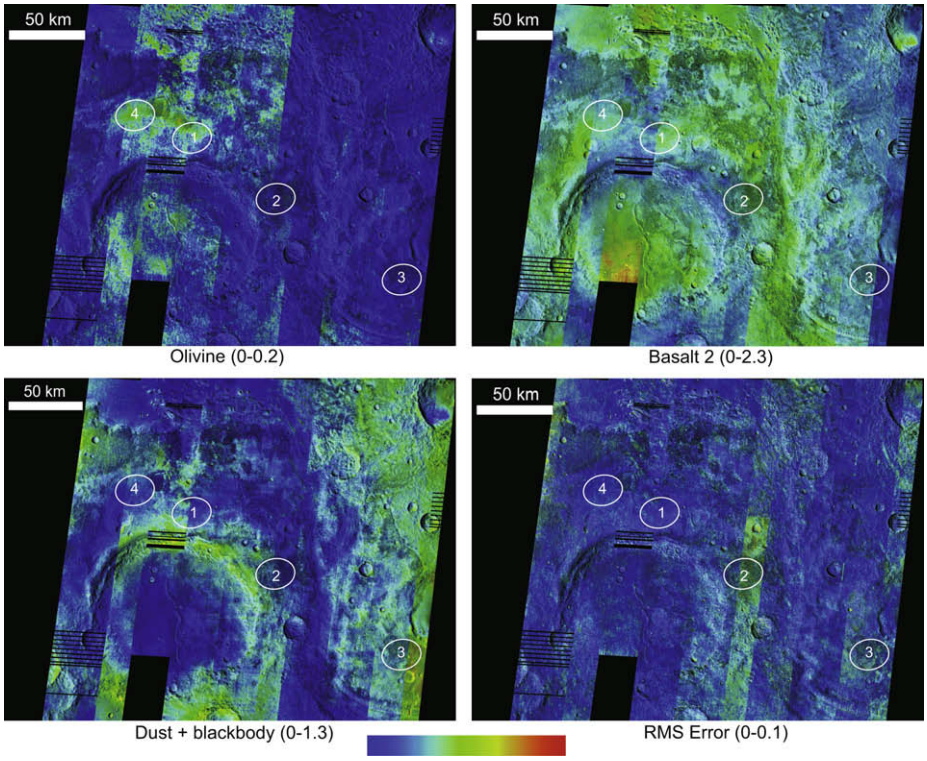

Fig. 14 (*continued*)

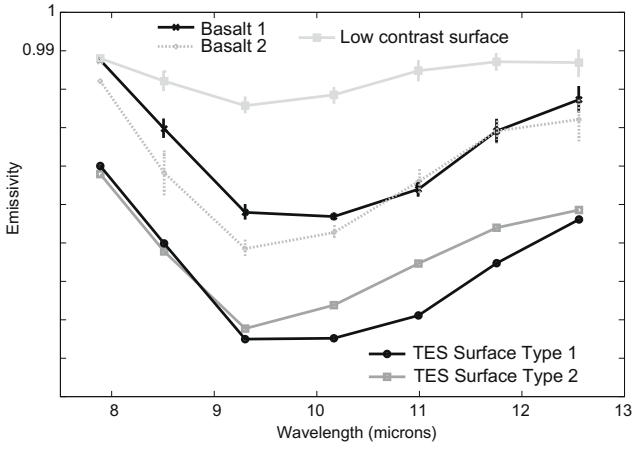

Fig. 15. THEMIS spectral end-members ("basalt 1" and "basalt 2") observed in the Mawrth Vallis region. The "low spectral contrast" spectrum is taken from an area of relatively high dust/blackbody concentration in Fig. 14b. TES surface types 1 and 2 are shown for comparison and are offset by −0.04 emissivity.

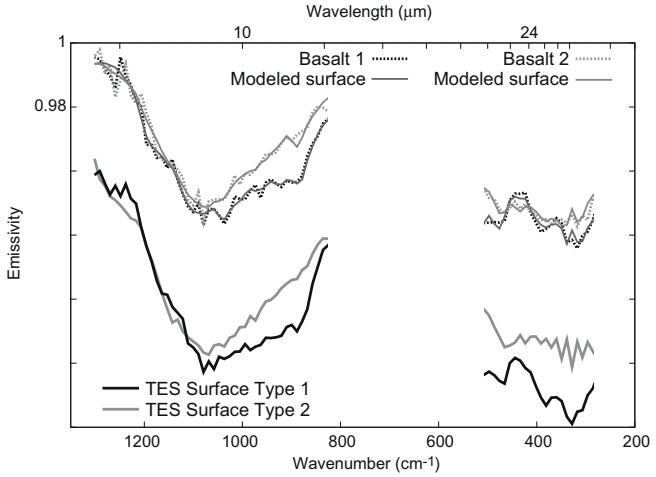

Fig. 16. TES surface emissivity spectra from the two major spectral units in the Mawrth Vallis region. TES surface types 1 and 2 are shown for comparison and are offset by −0.04 emissivity.

high-silica phases, phyllosilicate and non-phyllosilicate surfaces within the THEMIS basalt 2 unit are nearly identical mineralogically. The difference in high-silica phases is not large enough to produce significant differences in the 8–12 μm spectral region (Fig. 17), which explains why the phyllosilicate-bearing surfaces are not distinguished from non-phyllosilicate-bearing surfaces within the basalt 2 unit in THEMIS data.

The TES 465 cm^{-1} index exhibits moderate to high values (up to 1.02) in areas mapped as "basalt 2" in THEMIS data, and particularly high index values coincide with phyllosilicate regions. The 530 cm^{-1} index exhibits moderate values that coincide with areas mapped as "basalt 1" in THEMIS data (Fig. 18). Areas where both indices are present above the detection threshold are sparse throughout the study region, with little spatial coherence and almost no coincidence with phyllosilicate regions identified in OMEGA/CRISM data. One area where both indices are above the threshold values was selected for further spectral and quantitative mineralogical analysis. This region also coincides with a phyllosilicate-bearing surface identified by OMEGA/CRISM. The 465 cm^{-1} index is high (1.02), whereas the 530 cm^{-1} index value (1.007) is just above the threshold defined by Ruff and Christensen (2007) (1.005). A ratio of these spectra with those from a nearby bright region within the same orbit show little evidence for the smectite doublet (Fig. 19); however, Ruff and Hamilton (2009) suggest that a slight shoulder near 530 cm^{-1} in the ratio spectrum might indi-

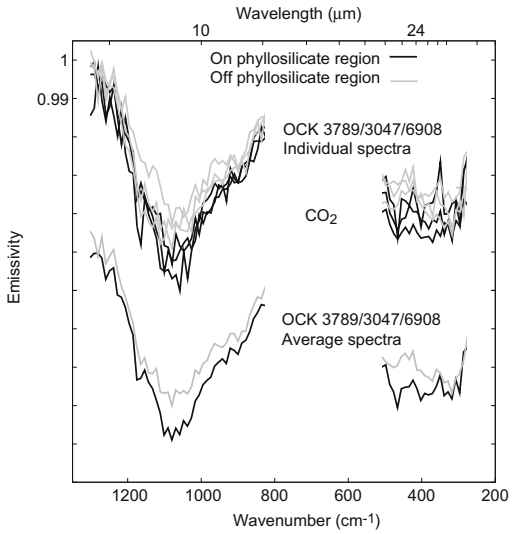

Fig. 17. TES surface emissivity spectra from three orbits that traverse phyllosilicate-bearing surfaces in Mawrth Vallis. Spectra from adjacent low-albedo surfaces are similar to phyllosilicate regions between ~800 and 1200 cm^{-1}, but significant differences are present at lower wavenumbers. The low wavenumber differences are due to 10–15% higher abundance of high-silica phases over phyllosilicate regions.

cate that the smectite abundance is near the index detection limit (10–20%).

Though the 530 cm^{-1} feature is questionable, the 465 cm^{-1} feature is strong in the ratio spectrum (Fig. 19). Linear least-squares modeling of the spectrum with high 465 and 530 cm^{-1} index values indicates that high-silica phases constitute more than 35% of the surface, similar to the high-silica phase abundance in TES surface type 2 (Bandfield et al., 2000b). Nearby surfaces covered by the same orbit are mineralogically similar, with the exception of high-silica phases, which are lower by ~15%. Thus the TES index and deconvolution analyses indicate that, in addition to the phyllosilicates detected by OMEGA/CRISM, the phyllosilicate regions also contain significant concentrations of a high-silica phase (>15%, possibly up to ~40%) that does not exhibit a smectite doublet, such as zeolite or amorphous silica. These conclusions are consistent with an independent assessment by Michalski and Fergason (2009). Trioctahedral smectites, such as saponite, are also candidate minerals for the strong 465 cm^{-1} feature. However, TES spectral modeling results indicate that amorphous silica and/or zeolite are the more likely high-silica phases producing the strong positive detections of the 465 cm^{-1} feature.

Phyllosilicate-bearing surfaces in Mawrth Vallis are extensive in area and are spatially resolvable with TES data. Thus the lack of a smectite doublet in the TES 465 and 530 cm^{-1} index data over OMEGA/CRISM phyllosilicate detections cannot be attributed to small outcrop size relative to the TES field of view. Rather, the discrepancy in detection between the thermal infrared and near-infrared wavelength regions must be due either to low phyllosilicate abundance (<10–20%, depending on the phyllosilicate composition) and/or texture/particle size effects. For the areas examined in detail with TES data, the surface emissivity is well modeled by coarse-particulate phases and exhibits spectral contrast typical of low-albedo regions. In addition, there is no apparent increase in dust/blackbody concentration corresponding with NIR phyllosilicate identifications (Fig. 14) that would indicate smaller particle sizes associated with the phyllosilicate regions. These observations are inconsistent with a dominant presence of fine particulate (<~60 μm) grains, suggesting that the 10–20% upper limits are a more likely explanation. We note that these estimates are inconsistent with abundances derived from OMEGA data by Poulet et al. (2008). For 10 isolated locations within the Mawrth Vallis phyllosilicate detections, Poulet et al. (2008) carefully selected single-pixel OMEGA spectra for non-linear unmixing modeling based on having the strongest phyllosilicate signatures in the region and a relatively sediment-free appearance in high-resolution visible images. For these spots, OMEGA-derived abundances were as high as 20–65% (±10%). The reason for the discrepancy is unclear, however it is possible that it is related to the difference in pixel resolution of each instrument (~0.6–3 km for OMEGA; ~3–8 km for TES). Thus there may be isolated locations (<~3 km^2 in area) within the Mawrth Vallis region that have phyllosilicate areal abundances as high as 65% (Poulet et al., 2008).

8. Miyamoto crater

Miyamoto, a ~150 km diameter crater located at ~352.0°E, 2.5°S, is partially buried by the southwestern margin of the Meridiani

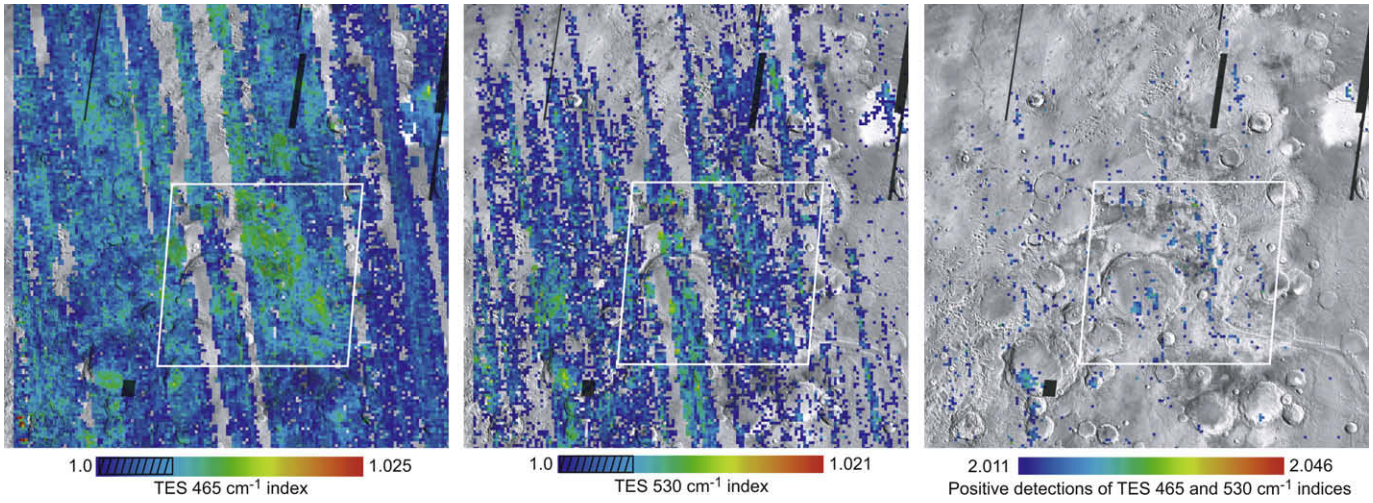

Fig. 18. TES 465 and 530 cm^{-1} index maps of the Mawrth Vallis region (20° to 30°N, 335° to 345°E), overlaid on a THEMIS daytime radiance mosaic. The hatched portion of the color scale bar indicates values that are below the index detection thresholds established by Ruff and Christensen (2007) (1.006 for the 465 cm^{-1} index, 1.005 for the 530 cm^{-1} index). Maps of "positive detections" of both indices represent the sum value of both indices for each pixel, and are masked where either index is below their respective detection threshold. The white polygon shows the location of the spectral unit mosaics from Fig. 14b.

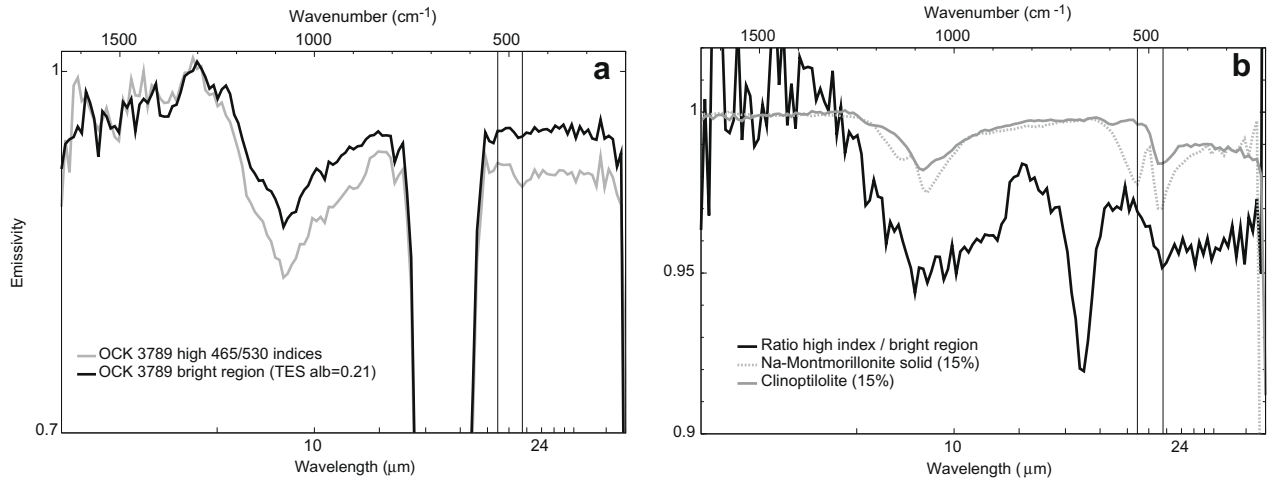

Fig. 19. (a) Spectra used in ratio for (b). (b) Ratio of TES spectra from a surface with a "positive" 465 and 530 cm^{-1} index detection (TES OCK 3789, ICK 1984 detector 6, ICK 1986 detector 6 and ICK 1987 detector 2) and a nearby surface with negative detections of both indices (TES OCK 3789, ICK 2006 detector 5, ICK 2007 detectors 2 and 6 and ICK 2008 detector 3). The ratio is compared with a scaled montmorillonite spectrum and zeolite spectrum. Vertical lines show the position of 465 and 530 cm^{-1} in both (a) and (b).

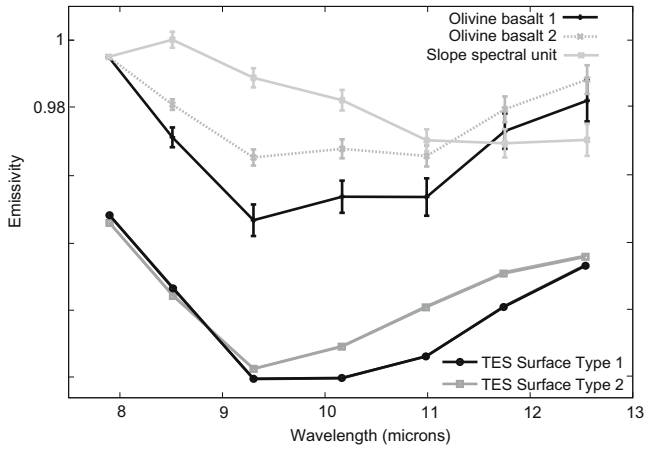

Fig. 20. THEMIS spectral end-members ("olivine basalt 1" and "olivine basalt 2") observed in the region of Miyamoto crater. TES surface types 1 and 2 are shown for comparison and are offset by −0.05 emissivity. Within the wavelength range covered by THEMIS, the hematite-rich unit does not contain features distinct from the other three compositional units, so no end-member for the hematite unit is shown here. The hematite-rich unit is distinguished in TES data (Fig. 21).

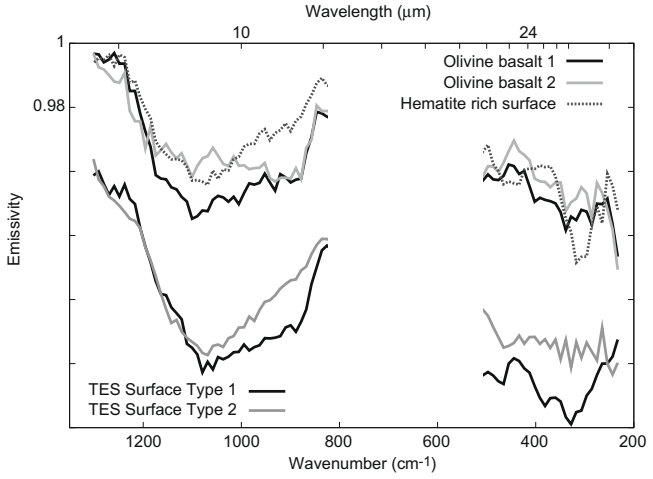

Fig. 21. TES surface emissivity spectra from the three major non-dust spectral units in Miyamoto crater. TES surface types 1 and 2 are shown for comparison and are offset by −0.04 emissivity.

Planum formation. The crater floor contains layered units as well as Fe–Mg phyllosilicate minerals identified from CRISM data (Newsom, H., 2008. The Miyamoto Crater Floor Landing Site, presentation at the 3rd MSL Landing Site Workshop, Monrovia, CA. Available from: <http://marsoweb.nas.nasa.gov/ landingsites/msl2009/workshops/3rd_workshop/program.html/>). Curved ridges that may be inverted channels have been cited as additional evidence for sustained aqueous activity in the region (Newsom, H., 2008. The Miyamoto Crater Floor Landing Site, presentation at the 3rd MSL Landing Site Workshop, Monrovia, CA. Available from: <http://marsoweb.nas.nasa.gov/ landingsites/msl2009/workshops/3rd_workshop/program.html/>).

There are four spectral units present in the TES and THEMIS data over Miyamoto crater and the surrounding plains (Figs. 20 and 21). Hematite-rich surfaces are located ~20–30 km to the northeast of the primary landing ellipse and are associated with the Meridiani Planum formation. These surfaces are dominated by pyroxene, high-silica phases, plagioclase, and hematite (Table 4). Slightly elevated sulfate abundances may also be present. The spectral shapes and derived mineralogies are similar to hematite-rich surfaces throughout the Meridiani Planum region. Hematite is spectrally featureless in the THEMIS spectral range. The inclusion of a blackbody end-member in the library used for spectral unit mapping accounts for spectral contrast variations due to the presence/absence of hematite. As described for the other landing sites, blackbody variations may also indicate variations in dust cover or particle size within the spectral units.

The region within and immediately surrounding the landing ellipse is characterized by a basaltic spectral shape in THEMIS data. The basaltic shape is somewhat variable within the region (Figs. 20 and 21), consistent with variable concentrations of olivine and high-silica phases and possibly sulfate minerals. To account for this variability, two basaltic shapes were used as end-members, however, these spectral differences are subtle in the THEMIS data and their spatial distributions are not well separated. Because of this, they have been combined into a single unit map (Fig. 22). The basaltic surfaces commonly contain significant amounts of pyroxene, plagioclase, high-silica phases, and olivine (Table 4).

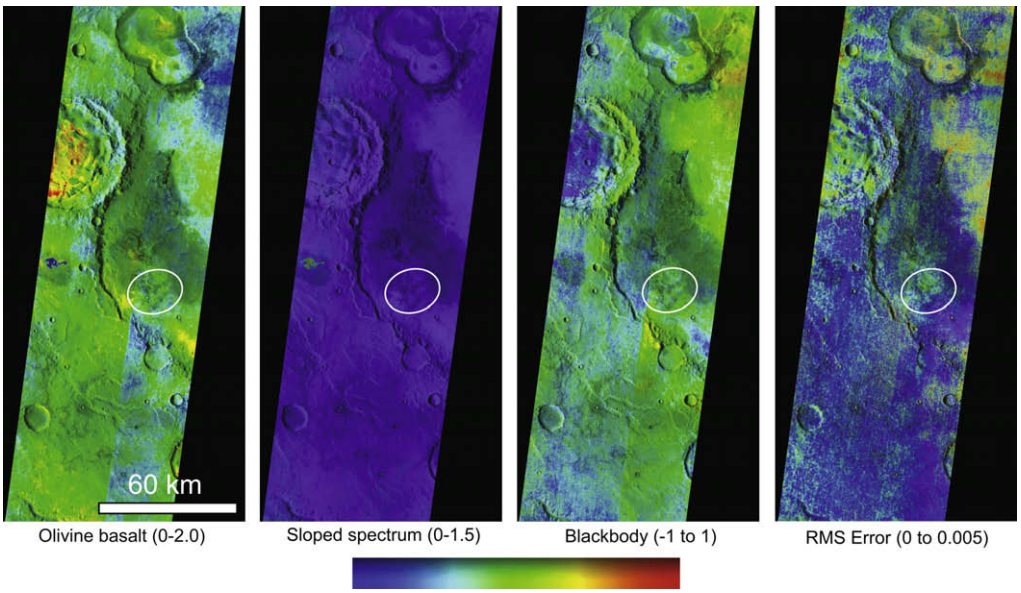

Fig. 22. THEMIS spectral unit distributions in Miyamoto crater (−5.0° to −1.3°N, 351.17° to 352.9°E). Map explanations are the same as in Fig. 2. Spatial variations in blackbody abundance are due to contributions from hematite and may also indicate varying particle size/textural variations.

A fourth spectral unit is located ~40 km west of the center of the primary landing ellipse (Fig. 22). This consists of a distinct spectral slope that has been attributed to the presence of chlorides (Osterloo et al., 2008) (Fig. 20). While this compositional interpretation is not certain, the surface is quite distinct and is similar to other exposures elsewhere on the planet that are characterized by a slightly higher albedo than the surrounding terrain, high thermal inertia, and irregular polygonal type textures in high-resolution imagery (<3 m/pixel).

Neither of the TES 465 nor 530 cm^{-1} indices display large values in or near the landing ellipse. Where slightly elevated values do occur, they indicate perhaps the presence of minor olivine and high-silica phases consistent with deconvolution results. Abundant hematite greatly affects 465 cm^{-1} index values and the distribution of hematite clearly dominates the 465 cm^{-1} index map (Ruff and Christensen, 2007).

TES albedo and DCI values, as well as the 8–12 μm spectral feature depth in TES and THEMIS data indicate that significant deposits of dust are not likely to be present throughout the Miyamoto crater region, thus dust was not included as an image end-member in the library used for spectral unit mapping. Significant deposits appear to be present to the north, outside of the immediate investigation region, however.

9. South Meridiani Planum

Located ~140 km east of the Miyamoto candidate ellipse, the proposed south Meridiani Planum landing ellipse is adjacent to the contact between the southern margin of the Meridiani Planum hematite-bearing plains unit and the Noachian cratered highlands. Phyllosilicate minerals identified with CRISM data are associated with polygonally fractured bedrock, in contact with overlying sulfate-bearing units associated with the hematite-bearing plains. The phyllosilicate deposits are dissected by putative fluvial features (Arvidson, R., Wiseman, S., the CRISM team, 2008. Candidate MSL Landing Site: Southern Meridiani Phyllosilicate/Sulfate Contact, MSL Steering Committee Presentations. Available from: <http://marsoweb.nas.nasa.gov/landingsites/>). The science rationale for this landing region is to sample a diverse suite of minerals associated with aqueous environments, within a stratigraphic context that is relatively well-defined from orbital measurements.

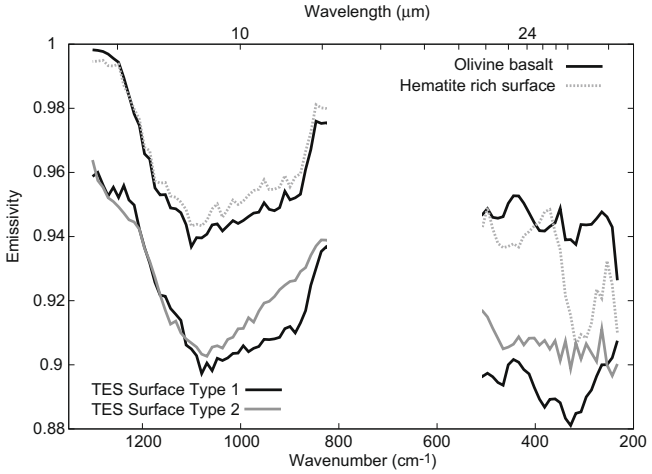

Fig. 23. TES surface emissivity spectra from the two major non-dust spectral units in south Meridiani Planum. TES surface types 1 and 2 are shown for comparison and are offset by −0.04 emissivity.

As with nearby Miyamoto crater, both TES and THEMIS data indicate that significant deposits of dust are not likely to be present throughout the south Meridiani region. There are two basic spectral units present in the TES data (Fig. 23). Hematite-rich surfaces are located within and generally to the north of the landing ellipse. These surfaces are dominated by pyroxene, plagioclase, hematite, high-silica phases, and olivine (Table 4). Slightly elevated sulfate abundances may also be present. The spectral shapes and derived mineralogies are similar to hematite-rich surfaces throughout the Meridiani Planum region. As described for Miyamoto crater, increases in blackbody abundance at THEMIS resolution indicate either increased hematite or dust abundance, or decreases in particle size.

The region surrounding the landing ellipse towards the south, west, and east is characterized by olivine basaltic compositions with some variability in composition similar to that present in Miyamoto crater (Fig. 24). The differences between these compositions are subtle in both the TES and THEMIS data and are not well separated. Because of this, they have been combined into a single

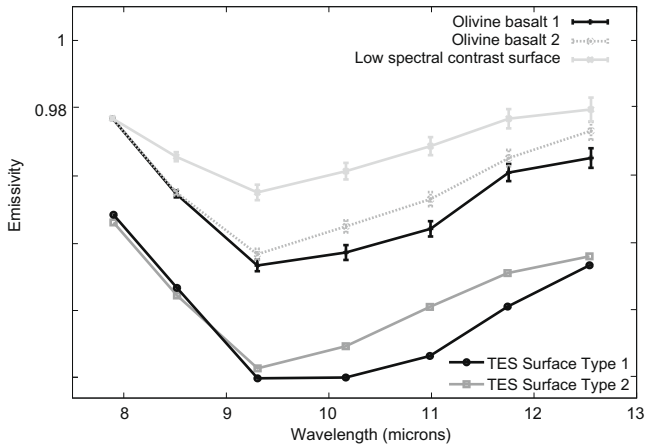

Fig. 24. THEMIS spectral end-members ("olivine basalt 1" and "olivine basalt 2") observed in the region of south Meridiani Planum. TES surface types 1 and 2 are shown for comparison and are offset by −0.05 emissivity. Within the wavelength range covered by THEMIS, the hematite-rich unit does not contain features distinct from the other compositional unit, so no end-member for the hematite unit is shown here. The hematite-rich unit is distinguished in TES data (Fig. 23).

unit map (Fig. 25). These differences may be indicative of variations in the concentration of high-silica phases relative to olivine and/or pyroxene concentrations. Once normalized for hematite, the two unit compositions are indistinguishable.

The presence of abundant hematite near the ellipse interferes with smectite detection using the TES index method. Elevated 465 cm^{-1} index values are present near the landing ellipse as expected due to the large hematite concentrations. Elevated 530 cm^{-1} index values are coincident with low-albedo basaltic surfaces to the south outside of the region of the landing ellipse, consistent with the presence of olivine.

10. Discussion

The dominant phases in all of the proposed landing regions are plagioclase, pyroxene, high-silica phases, olivine and perhaps minor abundances of sulfates. The relative abundances of these phases and the thermal infrared spectral properties of these surfaces are typical of most martian low-albedo regions (e.g., Bandfield et al., 2000b; Rogers et al., 2007). With the exception of silica-rich surfaces in Mawrth Vallis, dusty surfaces in Gale crater, and perhaps pyroxene-rich units in Holden crater ("olivine basalt 2"), it is expected that the surfaces analyzed by MSL will be dominated by compositions similar to what is observed in most other low-albedo regions. Thus in addition to characterizing the depositional environment of secondary minerals, the scientific payload on MSL will be positioned to provide important information about surface materials in typical low-albedo regions as well.

Evidence for phyllosilicates and/or sulfates has been identified using NIR spectroscopic measurements at all of the proposed landing sites presented here (3rd MSL Workshop, http://marsoweb.nas.nasa.gov/landingsites/index.html). Why are sulfate and phyllosilicate minerals detected from NIR measurements whereas little evidence for these minerals is present in the TIR data? For the sites where phyllosilicate minerals are dispersed in relatively small outcrops, the difference in spatial resolution between TES and CRISM is likely one contributing factor. However, phyllosilicate mineral distributions are extensive enough in Mawrth Vallis and Nili Fossae that spatial resolution cannot explain the differences. It is possible to resolve the apparent disparity of the NIR and TIR mineralogical results by considering the respective sensitivities of the two wavelength regions; NIR data are typically highly non-linear and sensitive to iron-bearing and hydrated mineralogies whereas the TIR data are generally sensitive to the bulk surface composition. If high concentrations of phyllosilicates and sulfates were present across the surface, a local decrease in the concentration of basaltic minerals would be evident in the TIR-derived unit maps. A local decrease would be present even if the other materials were somehow undetected due to, for example, fine particle sizes. Basalt unit maps do not show any such decrease in abundance corresponding with phyllosilicate regions. Similarly, blackbody/dust abundance does not increase over phyllosilicate regions in Mawrth Vallis and Nili Fossae. The TIR data clearly show that phyllosilicates are probably not present at concentrations greater than ~10–20% in Mawrth Vallis and Nili Fossae. Relatively small outcrop sizes in the other sites preclude a confident estimate of phyllosilicate concentration from TIR observations, however the NIR phyllosilicate signatures do tend to be weaker in these small outcrops (e.g., Milliken, R.E., 2008. CRISM Results for Eberswalde Crater, presentation at the 3rd MSL Landing Site Workshop, Monrovia, CA. Available from: <http://marsoweb.nas.nasa.gov/landingsites/msl2009/workshops/3rd_workshop/program.html/>), perhaps suggesting a lower concentration than those of Mawrth Vallis and Nili Fossae.

This information has several important implications for the MSL mission. If the materials of interest are distributed relatively evenly

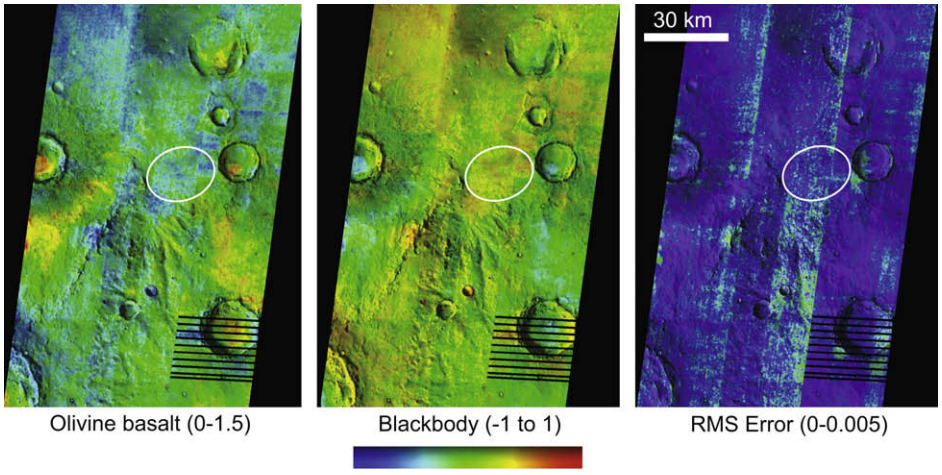

Fig. 25. THEMIS spectral unit distributions in the south Meridiani Planum region. Area shown is −4°N to −2°N, −7.0° to −4.6°E. Map explanations are the same as in Fig. 2. Spatial variations in blackbody abundance are due to contributions from hematite and may also indicate varying particle size/textural variations.

throughout the landing site, it may be difficult for the MSL payload to clearly identify the source of the mineralogical signatures from orbit. Hydrated minerals present in abundances as low as 5% could yield the 1.9 μm hydration feature, depending on the surface porosity and host composition of the hydrated materials (Poulet et al., 2007). Furthermore, orbital signatures are representative of the upper few tens of microns only; the volume abundance of phyllosilicate minerals, which may be present as thin coatings, could be even lower. Based on the available data from orbit, it is a realistic possibility that phyllosilicate minerals constitute a very small percentage of the volume of surface material. The abundances may be low enough that they present a challenge for clear identification from some of the instruments on MSL.

The fact that the bulk of the surface materials appear relatively unweathered and not distinct from many other regions indicates that the presence of liquid water at these sites may have been somewhat limited despite the presence of phyllosilicates. Although this scenario is a distinct possibility that would have a major negative impact on the astrobiological potential of those sites, it is also possible that the bulk surface materials are partially obscuring higher concentrations of the materials of interest (e.g., Poulet et al., 2008) that could be more clearly identified and sampled in-situ.

The spectral unit mosaics presented here represent a new method of THEMIS data analysis, which may be applied to other sites of interest. These maps provide very high resolution distributions of surface composition over relatively large areas. Unlike DCS mosaics, spectral unit maps provide more straightforward and quantitative representations of end-member distributions, and are less affected by atmospheric or temperature variations from one image to the next.

11. Summary

1. With the exception of Gale crater, all of the landing sites have relatively low dust cover compared to classic high-albedo regions and to previous landing sites in Gusev Crater, Utopia Planitia, and Chryse Planitia (Golombek et al., 2003).
2. The dominant phases in all of the proposed landing regions are plagioclase, pyroxene, high-silica phases, olivine and perhaps minor abundances of sulfates. The relative abundances of these phases and thermal infrared spectral properties of most of these surfaces (excluding silica-rich surfaces in Mawrth Vallis, dust-covered surfaces in Gale crater and perhaps pyroxene-rich units in Holden crater) are typical of most martian low-albedo regions (e.g., Bandfield et al., 2000b; Rogers et al., 2007) and represent relatively unweathered materials. The MSL scientific payload will thus be able to provide important information on surface materials typical of low-albedo regions.
3. Smectite minerals are not detected unambiguously for any of the candidate landing regions, using either TES spectral index or deconvolution analysis methods. The lack of a smectite doublet in TES 465 and 530 cm^{-1} index data over some of the candidate landing regions can be at least partially attributed to small phyllosilicate outcrop sizes relative to the TES field of view. Non-detections may also be attributed to (1) low phyllosilicate abundance (<10–20%, depending on the phyllosilicate composition) and/or (2) porous texture and/or small particle size (<~60 μm) associated with the phyllosilicate-bearing surfaces. In Mawrth Vallis and Nili Fossae, where phyllosilicate detections are relatively extensive in area, decreases in the concentration of basaltic minerals corresponding with those phyllosilicate detections are not observed. This indicates that phyllosilicate minerals are present in low abundance (<10–20 areal %), and suggests that the bulk of the surface material is relatively unweathered. However, it is possible that these relatively unweathered materials are partially obscuring higher concentrations of phyllosilicate minerals (e.g., Poulet et al., 2008) that could be sampled in-situ.
4. Two spectral units are observed within Nili Fossae, which are both classified as basalts based on TES-derived mineral abundances. Subtle variations in olivine, pyroxene and high-silica phases give rise to the spectral differences between the two units.
5. The proposed landing ellipse in Gale crater is dominated by surface dust with olivine basalt sand at the margin of the ellipse.
6. The floor of Holden crater is dominated by an olivine basaltic composition, which contains a minor amount of high-silica phases that could be secondary in nature. A less extensive spectral unit is found in small outcrops near the mouth of Uzboi Vallis. The unit is also olivine basaltic in nature, but with slightly higher pyroxene and/or olivine abundance and a less abundant high-silica phase.
7. The floor of Eberswalde crater and the surrounding plains are olivine basaltic in composition, with little variability within the region.
8. Two spectral units, which are spectrally similar to TES surface types 1 and 2 (Bandfield et al., 2000b), are present in Mawrth Vallis. These units are primarily distinguished by differences in olivine, pyroxene and high-silica phase abundance. The unit with the greater abundance of high-silica phases contains the phyllosilicate regions identified with OMEGA and CRISM data.
9. TES data over Mawrth Vallis indicate that phyllosilicate-bearing surfaces identified with OMEGA and CRISM data also contain significant concentrations (>15%, possibly up to ~40%) of a high-silica phase that does not exhibit a dioctahedral smectite doublet, such as zeolite or amorphous silica. Saponite is a possible, but less likely candidate for the additional high-silica phase. High-silica phase abundance over phyllosilicate-bearing surfaces is higher than that of surrounding surfaces by 10–15%.
10. Both the Miyamoto and south Meridiani candidate regions are dominated by hematite and basaltic or olivine basaltic compositional units.

Acknowledgments

We thank Matt Golombek, Frank Seelos, Olivier S. Barnouin-Jha, and Ralph Milliken for helpful discussions. This work was funded by the Critical Data Products Initiative for MSL Landing Site Characterization through the Jet Propulsion Laboratory. Steve Ruff and an anonymous reviewer provided comments that helped to significantly clarify this manuscript. THEMIS images are courtesy of NASA/JPL/Arizona State University.

References

Bandfield, J.L., 2002. Global mineral distributions on Mars. J. Geophys. Res. – Planets 107, 5042.

Bandfield, J.L., Smith, M.D., 2003. Multiple emission angle surface–atmosphere separations of Thermal Emission Spectrometer data. Icarus 161, 47–65.

Bandfield, J.L., Christensen, P.R., Smith, M.D., 2000a. Spectral data set factor analysis and end-member recovery: Application to analysis of martian atmospheric particulates. J. Geophys. Res. – Planets 105, 9573–9587.

Bandfield, J.L., Hamilton, V.E., Christensen, P.R., 2000b. A global view of martian surface compositions from MGS-TES. Science 287, 1626–1630.

Bandfield, J.L., Rogers, D., Smith, M.D., Christensen, P.R., 2004. Atmospheric correction and surface spectral unit mapping using Thermal Emission Imaging System data. J. Geophys. Res. – Planets 109. E10008. doi:10.1029/2004JE002289.

Bibring, J.P., Langevin, Y., Gendrin, A., Gondet, B., Poulet, F., Berthe, M., Soufflot, A., Arvidson, R., Mangold, N., Mustard, J., Drossart, P., Team, O., 2005. Mars surface diversity as revealed by the OMEGA/Mars Express observations. Science 307, 1576–1581.

Christensen, P.R., Anderson, D.L., Chase, S.C., Clark, R.N., Kieffer, H.H., Malin, M.C., Pearl, J.C., Carpenter, J., Bandiera, N., Brown, F.G., Silverman, S., 1992. Thermal Emission Spectrometer experiment—Mars-Observer Mission. J. Geophys. Res.—Planets 97, 7719–7734.

Christensen, P.R., Bandfield, J.L., Clark, R.N., Edgett, K.S., Hamilton, V.E., Hoefen, T., Kieffer, H.H., Kuzmin, R.O., Lane, M.D., Malin, M.C., Morris, R.V., Pearl, J.C., Pearson, R., Roush, T.L., Ruff, S.W., Smith, M.D., 2000a. Detection of crystalline hematite mineralization on Mars by the Thermal Emission Spectrometer: Evidence for near-surface water. J. Geophys. Res.—Planets 105, 9623–9642.

Christensen, P.R., Bandfield, J.L., Hamilton, V.E., Howard, D.A., Lane, M.D., Piatek, J.L., Ruff, S.W., Stefanov, W.L., 2000b. A thermal emission spectral library of rock-forming minerals. J. Geophys. Res.—Planets 105 (E4), 9735–9739.

Christensen, P.R., Bandfield, J.L., Hamilton, V.E., Ruff, S.W., Kieffer, H.H., Titus, T.N., Malin, M.C., Morris, R.V., Lane, M.D., Clark, R.L., Jakosky, B.M., Mellon, M.T., Pearl, J.C., Conrath, B.J., Smith, M.D., Clancy, R.T., Kuzmin, R.O., Roush, T., Mehall, G.L., Gorelick, N., Bender, K., Murray, K., Dason, S., Greene, E., Silverman, S., Greenfield, M., 2001. Mars Global Surveyor Thermal Emission Spectrometer experiment: Investigation description and surface science results. J. Geophys. Res.—Planets 106, 23823–23871.

Christensen, P.R., Jakosky, B., Kieffer, H.H., Malin, M.C., McSween, H.Y., Nealson, K., Mehall, G.L., Silverman, S.H., Ferry, S., Caplinger, M., Ravine, M., 2004. The Thermal Emission Imaging System (THEMIS) for the Mars 2001 Odyssey Mission. Space Sci. Rev. 110, 85–130.

Gillespie, A.R., Kahle, A.B., Walker, R.E., 1986. Color enhancement of highly correlated images. I. Decorrelation and HSI contrast stretches. Remote Sens. Environ. 20, 209–235.

Glotch, T.D., Morris, R.V., Christensen, P.R., Sharp, T.G., 2004. Effect of precursor mineralogy on the thermal infrared emission spectra of hematite: Application to martian hematite mineralization. J. Geophys. Res.—Planets 109. doi:10.1029/2003JE002224.

Golombek, M.P., Grant, J.A., Parker, T.J., Kass, D.M., Crisp, J.A., Squyres, S.W., Haldemann, A.F.C., Adler, M., Lee, W.J., Bridges, N.T., Arvidson, R.E., Carr, M.H., Kirk, R.L., Knocke, P.C., Roncoli, R.B., Weitz, C.M., Schofield, J.T., Zurek, R.W., Christensen, P.R., Fergason, R.L., Anderson, F.S., Rice, J.W., 2003. Selection of the Mars Exploration Rover landing sites. J. Geophys. Res.—Planets 108. doi:2003JE002074.

Grant, J.A., Irwin, R.P., Grotzinger, J.P., Milliken, R.E., Tornabene, L.L., McEwen, A.S., Weitz, C.M., Squyres, S.W., Glotch, T.D., Thomson, B.J., 2008. HiRISE imaging of impact megabreccia and sub-meter aqueous strata in Holden crater, Mars. Geology 36, 195–198.

Hamilton, V.E., Christensen, P.R., 2005. Evidence for extensive, olivine-rich bedrock on Mars. Geology 33, 433–436.

Hoefen, T.M., Clark, R.N., Bandfield, J.L., Smith, M.D., Pearl, J.C., Christensen, P.R., 2003. Discovery of olivine in the Nili Fossae region of Mars. Science 302, 627–630.

Koeppen, W.C., Hamilton, V.E., 2008. Global distribution, composition, and abundance of olivine on the surface of Mars from thermal infrared data. J. Geophys. Res.—Planets 113. E05001.

Lawson, C.L., Hanson, R.J., 1974. Solving Least-Squares Problems. Prentice-Hall, Englewood Cliffs, NJ. 340 p..

Lewis, K.W., Aharonson, O., 2006. Stratigraphic analysis of the distributary fan in Eberswalde crater using stereo imagery. Journal of Geophysical Research-Planets 111 (E06). E06001.

Malin, M.C., Edgett, K.S., 2000. Sedimentary rocks of early Mars. Science 290, 1927–1937.

Malin, M.C., Edgett, K.S., 2003. Evidence for persistent flow and aqueous sedimentation on early Mars. Science 302, 1931–1934.

Michalski, J.R., Dobrea, E.Z.N., 2007. Evidence for a sedimentary origin of clay minerals in the Mawrth Vallis region, Mars. Geology 35, 951–954.

Michalski, J.R., Fergason, R.L., 2009. Composition and thermal inertia of the Mawrth Vallis region of Mars from TES and THEMIS data. Icarus 199, 25–48.

Michalski, J.R., Kraft, M.D., Diedrich, T., Sharp, T.G., Christensen, P.R., 2003. Thermal emission spectroscopy of the silica polymorphs and considerations for remote sensing of Mars. Geophys. Res. Lett. 30. doi:10.1029/2003GL018354.

Michalski, J.R., Kraft, M.D., Sharp, T.G., Williams, L.B., Christensen, P.R., 2005. Mineralogical constraints on the high-silica martian surface component observed by TES. Icarus 174, 161–177.

Michalski, J.R., Kraft, M.D., Sharp, T.G., Williams, L.B., Christensen, P.R., 2006. Emission spectroscopy of clay minerals and evidence for poorly crystalline aluminosilicates on Mars from thermal emission spectrometer data. J. Geophys. Res.- Planets 111, E03004.

Milliken, R.E., Edgett, K.S., Swayze, G., Clark, R.N., Thomson, B.J., Anderson, R., Bell, J.F., 2009. Clay and sulfate-bearing rocks in a stratigraphic sequence in gale crater, Lunar Planet. Sci. XV. Abstract #1479.

Murchie, S., Arvidson, R., Bedini, P., Beisser, K., Bibring, J.P., Bishop, J., Boldt, J., Cavender, P., Choo, T., Clancy, R.T., Darlington, E.H., Marais, D.D., Espiritu, R., Fort, D., Green, R., Guinness, E., Hayes, J., Hash, C., Heffernan, K., Hemmler, J., Heyler, G., Humm, D., Hutcheson, J., Izenberg, N., Lee, R., Lees, J., Lohr, D., Malaret, E., Martin, T., McGovern, J.A., McGuire, P., Morris, R., Mustard, J., Pelkey, S., Rhodes, E., Robinson, M., Roush, T., Schaefer, E., Seagrave, G., Seelos, F., Silverglate, P., Slavney, S., Smith, M., Shyong, W.J., Strohbehn, K., Taylor, H., Thompson, P., Tossman, B., Wirzburger, M., Wolff, M., 2007. Compact reconnaissance Imaging Spectrometer for Mars (CRISM) on Mars Reconnaissance Orbiter (MRO). J. Geophys. Res.—Planets 112. E05S03.

Mustard, J.F., Murchie, S.L., Pelkey, S.M., Ehlmann, B.L., Milliken, R.E., Grant, J.A., Bibring, J.P., Poulet, F., Bishop, J., Dobrea, E.N., Roach, L., Seelos, F., Arvidson, R.E., Wiseman, S., Green, R., Hash, C., Humm, D., Malaret, E., McGovern, J.A., Seelos, K., Clancy, T., Clark, R., Des Marais, D., Izenberg, N., Knudson, A., Langevin, Y., Martin, T., McGuire, P., Morris, R., Robinson, M., Roush, T., Smith, M., Swayze, G., Taylor, H., Titus, T., Wolff, M., 2008. Hydrated silicate minerals on Mars observed by the Mars Reconnaissance Orbiter CRISM instrument. Nature 454, 305–309.

Osterloo, M.M., Hamilton, V.E., Bandfield, J.L., Glotch, T.D., Baldridge, A.M., Christensen, P.R., Tornabene, L.L., Anderson, F.S., 2008. Chloride-bearing materials in the southern highlands of Mars. Science 319, 1651–1654.

Poulet, F., Bibring, J.P., Mustard, J.F., Gendrin, A., Mangold, N., Langevin, Y., Arvidson, R.E., Gondet, B., Gomez, C., Team, O., 2005. Phyllosilicates on Mars and implications for early martian climate. Nature 438, 623–627.

Poulet, F., Gomez, C., Bibring, J.P., Langevin, Y., Gondet, B., Pinet, P., Bellucci, G., Mustard, J., 2007. Martian surface mineralogy from Observatoire pour la Mineralogie, l'Eau, les Glaces et l'Activite on board the Mars Express spacecraft (OMEGA/MEx): Global mineral maps. J. Geophys. Res.–Planets 112. E08S02.

Poulet, F., Mangold, N., Loizeau, D., Bibring, J.P., Langevin, Y., Michalski, J., Gondet, B., 2008. Abundance of minerals in the phyllosilicate-rich units on Mars. Astron. Astrophys. 487, L41–U193.

Ramsey, M.S., Christensen, P.R., 1998. Mineral abundance determination: Quantitative deconvolution of thermal emission spectra. J. Geophys. Res.—Planets 103, 577–596.

Rogers, A.D., Aharonson, O., 2008. Mineralogical composition of sands in Meridiani Planum determined from MER data and comparison to orbital measurements. J. Geophys. Res.—Planets E06. E06S14. doi:10.1029/2007JE002995.

Rogers, A.D., Bandfield, J.L., Christensen, P.R., 2007. Global spectral classification of martian low-albedo regions with Mars Global Surveyor Thermal Emission Spectrometer (MGS-TES) data. J. Geophys. Res.—Planets 112. E02004.

Ruff, S.W., 2004. Spectral evidence for zeolite in the dust on Mars. Icarus 168, 131–143.

Ruff, S.W., Christensen, P.R., 2002. Bright and dark regions on Mars: Particle size and mineralogical characteristics based on Thermal Emission Spectrometer data. J. Geophys. Res.—Planets 107. doi:10.1029/2001JE001580.

Ruff, S.W., Christensen, P.R., 2007. Basaltic andesite, altered basalt, and a TES-based search for smectite clay minerals on Mars. Geophys. Res. Lett. 34. L10204.

Ruff, S.W., Hamilton, V.E., 2009. New insights into the nature of mineralogic alteration on Mars from orbiter, rover and laboratory data. Lunar Planet Sci. XL. Abstract 2160.

Schultz, R.A., Frey, H.V., 1990. A new survey of multiring impact basins on Mars. J. Geophys. Res.—Solid Earth Planets 95, 14175–14189.

Seelos, F.P.O.S., Barnouin-Jha, S.L. Murchie, 2008. MRO CRISM systematic investigation of the MSL candidate landing sites. Lunar Planet Sci. XXXIX. Abstract 2041.

Smith, M.D., Bandfield, J.L., Christensen, P.R., 2000. Separation of atmospheric and surface spectral features in Mars Global Surveyor Thermal Emission Spectrometer (TES) spectra. J. Geophys. Res.—Planets 105, 9589–9607.

Wyatt, M.B., Hamilton, V.E., McSween, H.Y., Christensen, P.R., Taylor, L.A., 2001. Analysis of terrestrial and martian volcanic compositions using thermal emission spectroscopy: 1. Determination of mineralogy, chemistry, and classification strategies. J. Geophys. Res.—Planets 106, 14711–14732.